JOURNAL OF GEOPHYSICAL RESEARCH, VOL. 108, NO. D4, 8367, doi:10.1029/2002JD002199, 2003

Seasonal changes in the transport of pollutants into the Arctic troposphere-model study

A. Klonecki,[1] P. Hess, L. Emmons, L. Smith, and J. Orlando
National Center for Atmospheric Research, Boulder, Colorado, USA

D. Blake
Department of Chemistry, University of California, Irvine, California, USA

Received 13 February 2002; revised 9 August 2002; accepted 13 November 2002; published 28 February 2003.

[1] In association with Tropospheric Ozone Production about the Spring Equinox (TOPSE) measurement campaign a regional episodic chemical transport model is used to study the seasonal mechanisms of transport of pollutants from their Northern Hemisphere emission regions into the remainder of the troposphere. The model simulates the strong seasonal cycle for CO and hydrocarbons that agrees well with TOPSE measurements. In this study we use the isentropic perspective to analyze transport during different seasons and from different emission regions. Simulations with diagnostic tracers are conducted to quantify (1) the contribution of different emission regions to tracer distribution and (2) the importance of cross-isentropic transport. In the high latitudes during winter, in agreement with previous studies, the European and Siberian emission sources are the largest contributors to the diagnostic tracer distributions in the lower troposphere due to large-scale circulation patterns, low temperatures at the source and presence of a cold stable boundary layer that facilitates diabatic cooling. North American emissions are located further south, often south of the polar front, and are on average emitted at higher potential temperatures. Owing to their predominant transport over the relatively warm Atlantic, they experience strong diabatic heating due to the general instability in the air column and heavy precipitation in the storm track. During the summer months the pollution from all emission regions is more likely to be diabatically transported to higher potential temperatures and diluted. In addition, direct transport of pollutants into the Arctic is less frequent during summer due to the differences in the large-scale circulation patterns. *INDEX TERMS:* 0365 Atmospheric Composition and Structure: Troposphere—composition and chemistry; 0368 Atmospheric Composition and Structure: Troposphere—constituent transport and chemistry; 3307 Meteorology and Atmospheric Dynamics: Boundary layer processes; 9315 Information Related to Geographic Region: Arctic region; *KEYWORDS:* Tropospheric transport, isentropic transport, Arctic haze, Arctic pollution

Citation: Klonecki, A., P. Hess, L. Emmons, L. Smith, J. Orlando, and D. Blake, Seasonal changes in the transport of pollutants into the Arctic troposphere-model study, *J. Geophys. Res.*, *108*(D4), 8367, doi:10.1029/2002JD002199, 2003.

1. Introduction

[2] A number of measurement studies conducted in remote locations north of the polar front indicate a dramatic seasonal variation in the concentration of pollutants originating from midlatitude industrial centers. Hydrocarbon (HC) concentrations reach a maximum during the winter months and decrease throughout the spring with a minimum during summer. Measurements taken during the TOPSE (Tropospheric Ozone Production about the Spring Equinox) campaign [*Atlas et al.*, 2003] over North America between 40°N and 85°N confirm this and show that the buildup of HCs maximizes at the high latitudes, well away from large emission sources. It has been suggested that with the return of sunlight in the spring the buildup of HCs initiates a "photochemical bloom" and subsequent rapid ozone production. One of the major objectives of the TOPSE campaign was to document the winter-spring transition in tropospheric photochemistry and to investigate the contribution of the possible bloom in chemistry to the observed spring ozone maximum.

[3] The seasonal increase in the concentration of pollutants has been especially well documented for the polar latitudes, where pronounced pollution events are frequently present during winter and spring. These events, which have come to be known as Arctic Haze, manifest themselves in sharp, episodic decreases in the visibility over the lower

[1]Now at NOVELTIS, Ramonville-Saint-Agne, France.

0148-0227/03/2002JD002199

troposphere. They are caused by large concentrations of aerosols thought to be primarily of anthropogenic origin. Due to its dramatic nature, Arctic Haze has been studied since the 1970s through a number of measurement programs [e.g., *Barrie and Hoff*, 1985; *Barrie et al.*, 1994]. Less documented is the seasonal buildup of HCs in the polar region (e.g., in Alaska [*Blake and Rowland*, 1986] and on Spitsbergen [*Solberg et al.*, 1996]), with a seasonality similar to that of Arctic Haze (i.e., maximum concentrations in winter or spring). The seasonality in HCs has also been documented to extend considerably to the south: studies in the Canadian boreal forest [e.g., *Jobson et al.*, 1994 and *Young et al.*, 1997], over the North Atlantic from aircraft measurements [*Penkett et al.*, 1993], and over North America during TOPSE [*Blake et al.*, 2003] have shown that the strong seasonality of HCs extends to midlatitudes. The amplitude of the cycle depends on the species and on the location.

[4] The wintertime buildup of HCs in the midlatitudes and pollution events in the arctic region (connected with Arctic Haze) are often treated separately and yet similar processes are at least partially responsible for both phenomena. Both are likely to be affected by the much slower wintertime removal rates of atmospheric constituents: wet removal in the case of aerosols, and oxidation by OH in the case of HCs. It has also been suggested that seasonal changes in the circulation of the lower troposphere cause large changes in pathways of pollutant transport. For example, *Barrie* [1986] argues that the maximum transport to the Arctic takes place in winter, while in summer this transport is much slower. In particular, as concluded from studies of Arctic Haze [e.g., *Raatz and Shaw*, 1984; *Barrie*, 1986], climatological circulation patterns result in strong winter and spring transport from Eurasia, but weak transport from North America.

[5] During the spring months there is a rapid transition from wintertime concentration distributions to those typical of the summer months. While changes in the photochemistry explain aspects of this transition, transport changes are also important. We use a three-dimensional chemical transport model to examine how seasonal changes in transport affect the springtime transition in chemical concentrations, and more importantly, how and why the transport pathways from midlatitude pollution sources to polar latitudes (hereafter referred to as the Arctic) differ with season. To isolate the effect of transport we introduced diagnostic tracers that are either passive or have a constant 7-day lifetime. To further investigate the transport events into the Arctic we analyze the transport pathways in relation to surfaces of constant potential temperature (isentropic surfaces). The isentropic methodology has been previously applied to studies connected with the Arctic Haze [e.g., *Carlson*, 1981; *Iversen*, 1984; *Raatz*, 1991] and represents a powerful mechanism to interpret the transport pathways into the high and midlatitudes and their change with season. In this work we expand on the earlier studies to show how the transport and distribution of polluted airmasses is affected by their cross-isentropic transport due to diabatic heating and cooling.

[6] The paper is organized as follows: section 2 gives the model description, section 3 examines the seasonality of measured and modeled tracers, section 4 analyzes the transport from an isentropic perspective. We present our conclusions in section 5.

2. Model Description

[7] The HANK regional chemical transport model is described in *Hess et al.* [2000] and only a brief description of the model setup is repeated here. More detailed descriptions of recent changes concerning wet-deposition, the chemistry mechanism, the emissions, the lightning production of NO_x, and the boundary conditions are given in the Appendix to this paper. HANK has been extensively evaluated in *Hess et al.* [2000] and *Hess* [2001].

[8] HANK is a chemical transport model (CTM) that belongs to a class of models often termed "off-line." These models do not calculate the dynamical fields themselves, but instead rely on meteorological models to provide fields necessary to describe the state of the atmosphere. HANK uses the fields calculated by the MM5 (Pennsylvania State/National Center for Atmospheric Research Mesoscale Modeling System [*Grell et al.*, 1993a]) for December 1999 through July 2000. Both MM5 and HANK use the Grell convective parameterization scheme [*Grell*, 1993] for deep and shallow convective transport, and the medium-range forecast model (MRF) counter gradient scheme [*Hong and Pan*, 1996] for diffusive and boundary layer mixing.

[9] In this study both the MM5 and HANK are configured to a polar stereographic grid with the North Pole in the middle of the domain and with an irregular southern border extending to at least 25°N (the domain is shown in Figure 17). This domain size allows simulation of transport from the primary emission regions in the midlatitudes to the Arctic. The horizontal resolution (at 60°N the grid size is 243 km) is coarse because of computational limitations for long integrations, while the vertical resolution is fine (39 levels on a hybrid sigma coordinate between the surface and 100 mb) so as to better represent the small-scale vertical tracer structure observed during previous campaigns [*Ridley et al.*, 1997].

[10] In this study HANK simulates the chemistry, transport, and dry and wet deposition of 56 chemical species. The chemical mechanism accounts for the chemistry of species that influence ozone production and the oxidizing capacity of the troposphere in general and includes the oxidation of the most important organic compounds that play an important role as secondary sources of CO. The initial starting conditions and the boundary conditions for chemical tracers were obtained from the global 3 dimensional MOZART (Model of OZone and Related Tracers) model [*Brasseur et al.*, 1998; Horowitz et al., A global simulation of tropospheric ozone and related tracers: Description and evaluation of MOZART, version 2, in preparation].

3. Seasonal Differences in the Distribution of CO, HCs and Modeled Diagnostic Tracers From January Through July 2000

[11] The TOPSE campaign provided an extensive and unique data set of the composition of the winter and spring troposphere between 40°N and 85°N. It consisted of a set of chemical measurements made on a series of aircraft flights from Broomfield (Colorado, 39.5°N, 105°W) to Thule

(Greenland, 76°N, 68.5°W) or Alert (Canadian Arctic, 82°N, 62°W) between February and late May 2000 [*Atlas et al.*, 2003]. We begin this section by evaluating the timing and magnitude of the simulated seasonal cycle of CO and HCs in HANK against the TOPSE measurements to establish that HANK captures many aspects of the seasonal transition in the TOPSE region. An evaluation of the performance of the model in simulating species that are not discussed in this article is given in Emmons et al. (The budget of tropospheric ozone during TOPSE from two CTM's, submitted to *Journal of Geophysical Research*, 2002). In summary, HANK's ozone compares well with the TOPSE measurements, while NO_x is generally too low in the Canadian Arctic. The model simulated OH concentrations are approximately 25% higher than the TOPSE measurements (the measurements are only available in the lower troposphere). While on average the photolysis rate of O_3 to $O(^1D)$ in HANK agrees with the measurements to within 5% overall, the water vapor in HANK (as input from the MM5) is approximately 20% too high. This demonstrates the important effect that meteorological errors can have on chemical simulations.

3.1. Seasonal Evolution of HCs During TOPSE - Simulation and Measurements

[12] Figure 1 shows the measured and modeled median mixing ratios for CO and for three hydrocarbons: ethene, propane and ethane. These three HCs were chosen because they were: 1) both measured and modeled, 2) they have significant surface emissions and 3) they span a range of chemical lifetimes from a few days to weeks. Both the model and measured data were sampled between 1 and 6 km, and are divided in Figure 1 into four latitude bands and the seven deployments of the TOPSE campaign: 1) February 4–9, 2) February 21–27, 3) March 5–8, 4) March 19–26, 5) April 2–11, 6) April 23–30, 7) May 15–23. The simulated concentrations are interpolated to the location and time of each measurement along the aircraft flight tracks. Although in certain locations and times the model error is large (e.g. CO is too low near the end of the campaign, ethane and propane too high during deployment 1 and 2), the modeled values are generally within 30% of the measured ones. The existing discrepancies are probably influenced to a large extent by the uncertainty in the model emissions and inadequate knowledge of the initial conditions. In addition the model overestimates OH (Emmons et al., submitted manuscript, 2002), which leads to a simulation in which the removal rate for CO and HCs is overestimated.

[13] Although the simulated CO and HC concentrations tend to be somewhat high initially, and at the end of the campaign too low, the model reproduces well the timing of the seasonal decrease in the measured concentrations. HANK also captures the relative maximum in measured CO, C_3H_8 and C_2H_6 during the fourth deployment. In agreement with the measurements the rapid concentration decrease in the short-lived ethene is simulated to occur early in the campaign, while in both the model and measurements the largest concentration decrease in CO, C_3H_8 and C_2H_6 does not occur until after the fourth mission. Note also that in both the model and measurements the seasonal decrease in the longer lived species (i.e., CO and ethane) is less pronounced than for the short-lived species. HANK also captures (Figure 1, right column) the transition between the initial strong latitudinal gradient in the species concentrations and the relatively flat latitudinal gradients measured later in the mission. HANK successfully simulates the latitudes where the species gradients are particularly strong and the difference in the gradients between species.

[14] A comparison of the modeled and measured vertical profiles of propane and CO for the last four deployments of the TOPSE campaign is depicted in Figure 2. These four deployments capture the large transition from winter to spring conditions. The lowest concentrations of propane were measured in the boundary layer during the ozone depletion events caused by halogen species as described by *Ridley et al.* [2003]. Chlorine, which is enhanced during ozone depletion episodes leads to increased oxidation of propane. As reactions of halogen species are not simulated in HANK, locations where measured ozone was below 30 ppbv were not included in Figure 2. However, despite this filtering, the measured boundary layer concentration of propane during deployment 4 is still anomalously low. It is possible these low propane concentrations are influenced by the outflow from ozone (and HC) depletion events, which are not captured by our simple filter. The model reproduces the seasonal change in the concentration and vertical structure of propane (with exception of the lowest km during deployment 4), capturing the transition between the relatively high vertical gradient measured during deployment 4 to the small vertical gradient present during deployment 7. Modeled and measured ethane and ethene exhibit similar behavior (not shown), except the transition takes place earlier for ethene as indicated in Figure 1. As discussed previously, the model underestimates CO during campaigns 5–7 (Figure 2b). The modeled and measured vertical profiles show, however, a similar vertical structure.

[15] Finally we compare the surface measurements of CO from the NOAA/CMDL network [*Novelli et al.*, 1998; revised mixing ratios provided by P.C. Novelli, personal communication, 2002] with the corresponding mixing ratios from the model. Figure 3 shows the comparison for stations located north of 50°N with model data sampled at the lowest model level and at times corresponding to the opening of the flasks for CO measurements. As with the aircraft data, the model overpredicts the mixing ratios in the beginning of the simulation and underestimates them near the end. However, the model simulates well the general trend in CO. In addition, for stations not affected by fresh emissions (stations in Alaska and Canadian Arctic), in most cases the model simulates well the timing and magnitude of episodic changes in the CO mixing ratios and correctly reproduces the rather small variability in the measured data. For stations that are directly impacted by fresh emissions, especially Mace Head and the Ocean Station M, the model also generally simulates well the timing of the pollution events, but tends to overestimate the peak values. For stations located south of 50°N (figure not shown), the model results show similar level of agreement with the observed data.

3.2. Simulations With Diagnostic Tracers

[16] The seasonal evolution of CO and HCs along the TOPSE flight paths is clearly strongly affected by the

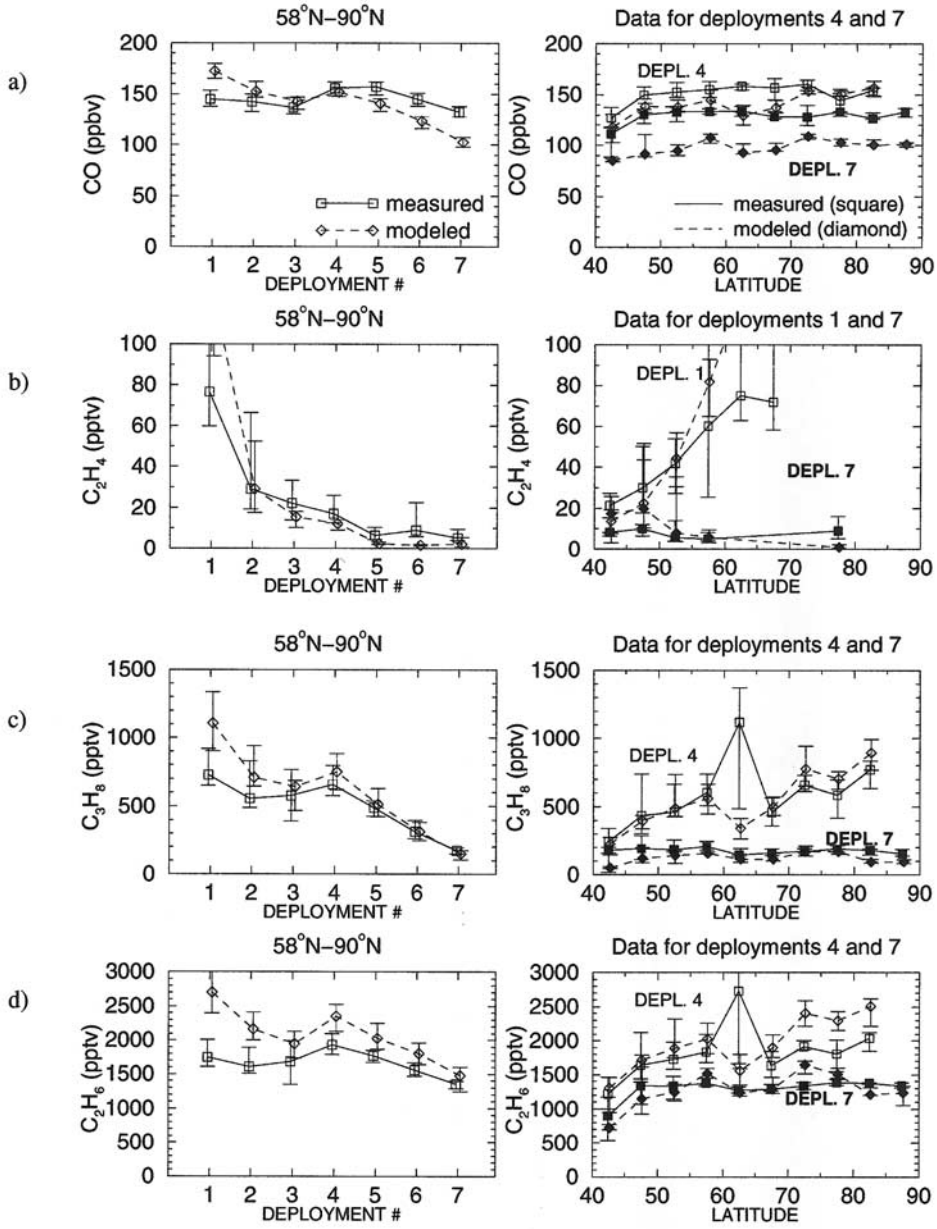

Figure 1. Comparison of the measured (solid line) and modeled (dashed line) median mixing ratios for (a) CO, (b) ethene, (c) propane, and (d) ethane for data sampled in the 1 to 6 km altitude range. Modeled data are interpolated spatially and temporally to the location and time of each measurement. The error bars indicate the ±25 percentiles. The figures in the left column show data sampled between 58°N and 90°N binned by deployment. The figures in the right column show data binned by latitude for two deployments: one just before the winter-spring transition (open symbols) and one after (filled symbols).

increasing rate of oxidation with the onset of spring. In addition, the seasonal cycle for each species is modified by: 1) the extent of its wintertime accumulation in the high latitudes, 2) the presence of secondary sources (e.g., the CO source from HC oxidation), 3) changes in source strength with season (e.g., seasonal changes in biomass burning emissions) and 4) changes in transport patterns from emission regions (for CO see *Lamarque and Hess* [2003]). In this work we investigate this last point: the role of seasonal changes in transport patterns on the distribution of pollutants in the mid and high latitudes. This paper does not attempt to quantify the relative effect of transport versus that of other mechanisms (e.g. chemistry) in accounting for the seasonal transition in species concentrations. Such an attribution would likely be different for each species considered. Instead, in the remainder of this section, we show with the use of idealized diagnostic tracers that seasonal changes in transport alone are important for the tracer distribution. Similarities in the distribution of the diagnostic tracers and those of CO and HCs suggest that the same seasonally changing transport mechanisms apply to both sets of species.

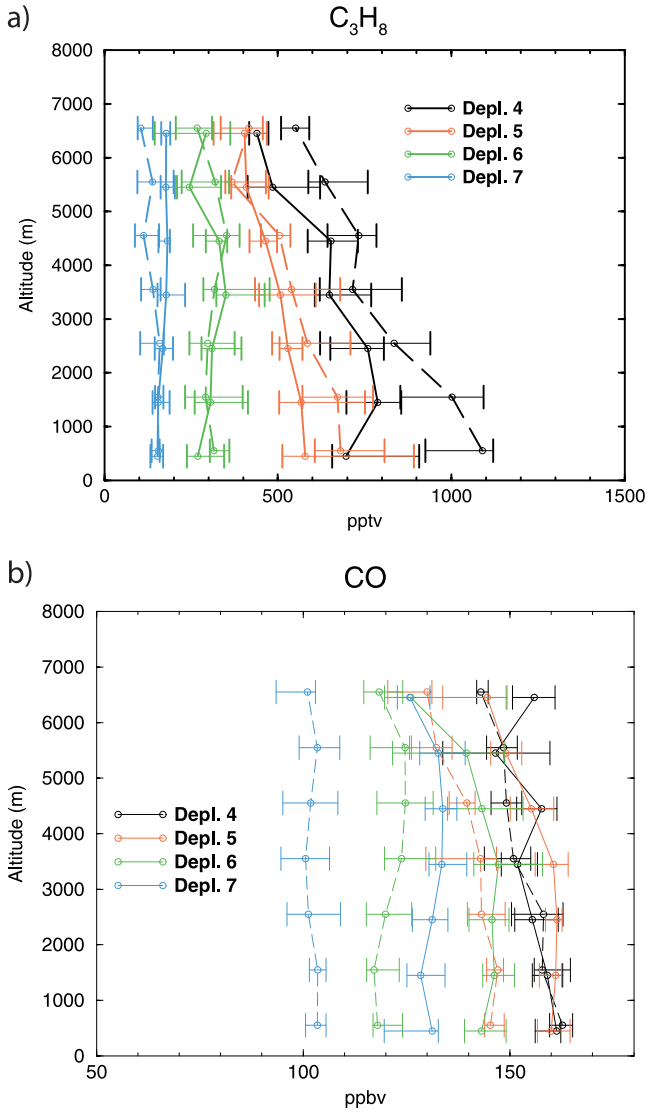

Figure 2. Measured (solid line) and modeled (dashed line) medians of (a) propane and (b) CO for deployments 4, 5, 6, and 7. Data are sampled north of 58°N and are binned by altitude.

[17] To isolate the role of transport from that of other mechanisms we introduce two diagnostic tracers: one with a 7-day decay time (TR7, to diagnose the direct transport of short-lived species from its emission source) and one entirely chemically passive tracer (TRN, to diagnose transport behavior in the longer term). Both of these species are assigned the same source, which, in order to compare results for different months, is constant in time. The source is equal to the CO emission source in December. The CO emission footprint is characteristic of most anthropogenic pollutants, so that the results will be generally applicable. The simulations, which are driven by MM5 derived fields (described in section 2), are carried out for three periods corresponding to winter, spring and summer. Each of these periods is two months long: 1) December (1999) and January (2000), 2) March and April (2000), and 3) June and July (2000). The first month from each of these periods is used for spinup. The results shown are taken only from the second month in each case (January, April and July). Note, that the differences in the distribution of these diagnostic tracers between the three seasons result only from differences in transport and not from the differences in chemistry or emissions. For all simulations the initial conditions and the boundary conditions are set to zero. The surface deposition is also set to zero.

3.2.1. Seasonality in the Simulated Distribution of Diagnostic and Chemical Tracers

[18] Figure 4 shows the zonally and monthly averaged vertical cross sections of the mixing ratio of the non-reactive tracer (TRN) simulated for January, April and July. The mean isentropic surfaces are also shown (see section 4). Clearly transport differences alone lead to a substantially different distribution between the seasons. The largest difference is in the high latitude lower troposphere, where the mixing ratios are more than a factor of two lower in July than in January. On the other hand, TRN is higher in July in the middle troposphere south of about 60°N and in the upper troposphere.

[19] For comparison, we examine in Figure 5 the simulated distribution of monthly and zonally averaged CO for January, April, and July from the runs with 56 chemical tracers. Sources of seasonal change other than transport (discussed above in section 3.2) clearly affect the seasonal cycle in CO, particularly the increase in oxidants with the end of winter (in January CO has a lifetime on the order of one month at low latitudes and is practically inert at high latitudes, while in July its lifetime is around 2 weeks in the low latitudes and one-two months in the high latitudes). Total flux of CO emitted in the model domain also changes from 41Tg in January and April to 56Tg in July. Nevertheless, there are similar features in the zonally averaged seasonal distribution of TRN and CO that point to the common role of transport. In winter a considerable fraction of both tracers is confined to the lowest 1 km, and the isolines are relatively horizontal there. In summer, on the other hand, the bulge in their midlatitude isolines suggests the common role and importance of vertical mixing. The distributions of both tracers also suggest significant near-surface transport to the Arctic during winter; during summer this near-surface transport is weaker and the highest concentrations in the Arctic are not located at the surface, but instead are simulated in the mid-troposphere.

[20] The seasonal change in the distribution of the vertically integrated mass of TRN is compared quantitatively in Figure 6. In agreement with conclusions from Arctic Haze studies, more of the tracer is shifted to higher latitudes during winter (Figure 6a). Figure 6b shows that, at all latitudes, significantly more of the tracer is contained in the lowest kilometer above the ground in winter than in summer and that the ratio of winter to summer concentrations increases with latitude. A similar result applies in the 1–3 km altitude band. The opposite is the case above 6 km, where the summertime concentrations are higher at all latitudes consistent with a higher rate of vertical mixing (Figure 6c). The corresponding plot for CO is shown in Figure 7. To account for the decrease in the summertime concentrations, the integrals are normalized by the total mass of CO present in the model during January and July. The normalized CO behaves very similarly to TRN. Again more of the CO is present in the high latitudes

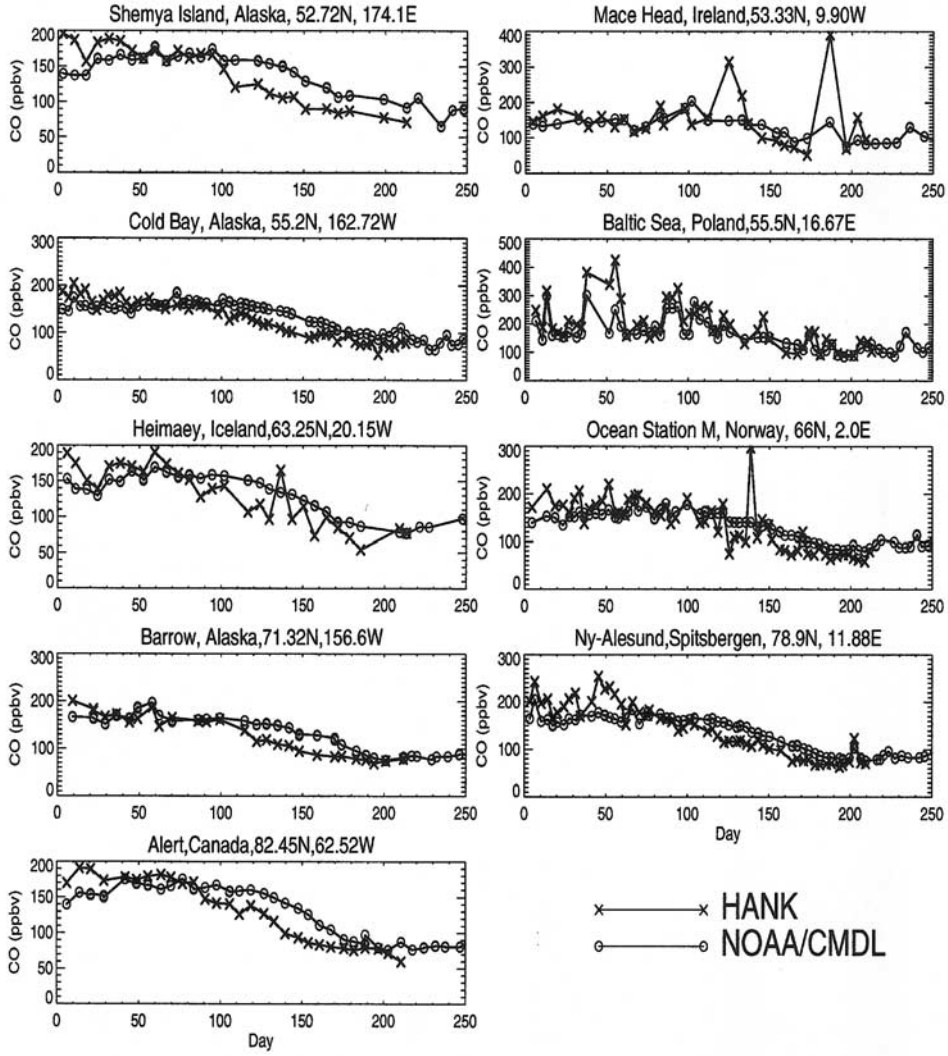

Figure 3. Measured values of CO from the CMDL network (open circles) and corresponding modeled values (crosses) for stations located north of 50°N.

during winter than summer (although this could also be driven by the weaker chemical removal rate in the high latitudes), and more is present in the lowest troposphere. In the upper troposphere in the midlatitudes more of the normalized CO is present in the summertime.

[21] Figure 8 shows the seasonal changes of the diagnostic tracer with the relatively short 7-day lifetime (TR7). The short lifetime emphasizes the shorter transport pathways and decreases the background concentrations.

[22] The overall transport characteristics of TR7 (Figure 8) are rather similar to the inert tracer although important differences remain. In particular, the seasonal cycle in TR7 is significantly larger than that of TRN in both the midlatitude free troposphere and in the high latitudes (compare Figures 4 and 8). Note that the TOPSE measurements also indicate the short-lived hydrocarbons have higher amplitude seasonal cycles than the longer-lived species. Differences in the isentropic distributions of TR7 and TRN are discussed in section 4.1.

[23] Figure 9 shows the simulated seasonal distribution of the short-lived ethene, which is compared here with TR7. Changes in the distribution of ethene must be largely driven by changes in its oxidation rate, but also by changes in its emissions (emissions within the model domain are 0.41Tg/C in January, 0.52Tg/C in April and 0.82Tg/C in July). Based on its reaction rate with OH, for which the rate constant shows little sensitivity to temperature and pressure, the lifetime of ethene is approximately 2 weeks for [OH] = 10^5 molec/cm^3 and 1.4 days for [OH] = 10^6 molec/cm^3. During winter the strong meridional gradient in OH is likely to be responsible for the free tropospheric meridional gradient of ethene. The corresponding gradient looks different for TR7, which is lost at the same rate in the high and low latitudes (7-day lifetime). The large decrease in C_2H_4 between winter and summer is also clearly driven by the increased rate of oxidation (compare with measurements in Figure 1). Nevertheless despite these differences, there are features that are common to the distributions of both C_2H_4 and TR7, suggesting the same seasonal transport changes impact both tracers. In the high latitudes, away from the primary emission regions, there is a pronounced seasonal change in the vertical gradient of both ethene and

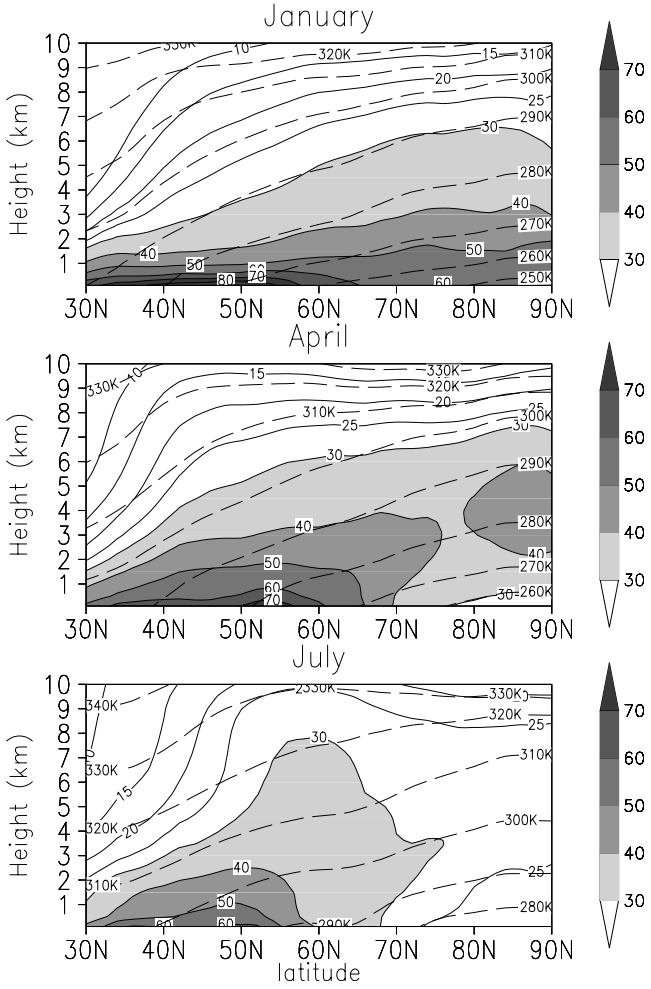

Figure 4. Monthly and zonally averaged mixing ratios of TRN for January, April, and July in ppbv (solid lines, values above 30 ppb are shaded). The dashed lines indicate the monthly and zonally averaged isentropes (K).

TR7. Also, as with the long-lived species, both TR7 and ethene are transported into the Arctic to a greater extent during winter than summer, and they are transported to the midlatitude free troposphere to a greater extent in summer than winter.

3.2.2. Seasonal Differences in the Impact of Emission Sources on the TOPSE Region

[24] The differences in seasonal distributions of trace species are partially due to changes in the influence of different emission regions. Here, with the help of diagnostic tracers labeled by region of emissions we quantify the contribution of the major emission regions and their change with season. We tag TRN and TR7 by one of five emission regions: 1) North America, 2) Eurasia west of 40°E (central and western Europe, hereafter referred to as the European source), 3) Eurasia east of 40°E and north of 45°N (referred to as the Siberian source), 4) Eurasia east of 40°E and south of 45°N (predominantly emissions from the Far East, the southeast Asian source), and 5) global emissions north of 45°N. Eurasia was split into 3 regions to differentiate between the large emissions in central and western Europe, the sparse but northern emission source over Siberia, and the high emissions located over China, Korea and Japan. The latitudinal distribution of the emissions in each of these regions is given in Table 1.

3.2.2.1. Winter Case

[25] Figure 10 shows the zonally and monthly averaged mixing ratios of TRN in January (upper left panel), and the contribution from each of the 5 emission regions to this averaged distribution. The simulation for January indicates that Europe contributes more than 50% to the total burden of TRN in the lower Arctic (Figure 10) compared to only 10–15% for North America, despite the relatively similar total source strength of the two regions (see Table 1). The contribution from the North American emissions increases with height, however, and becomes the dominant contributor to TRN in the upper troposphere. The distribution of emissions from these two sources is shown separately in Figure 11. The North American tracer is lifted upwards as it is transported northward, roughly following the slope of the isentropes (see section 4). The European tracer, by contrast, is transported northward near the surface.

[26] The SE Asian emissions of TRN, although large, contribute relatively little to the overall concentrations of TRN in the mid- and high- latitudes in agreement with the

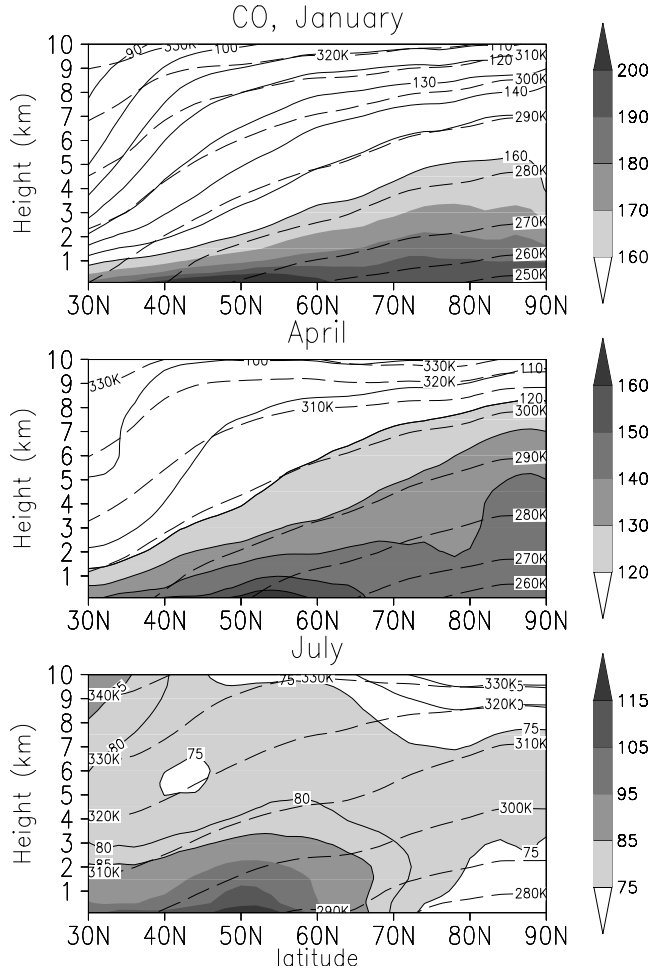

Figure 5. Monthly and zonally averaged mixing ratios of modeled CO for January, April, and July in ppbv (solid lines and shaded areas). The dashed lines indicate the monthly and zonally averaged isentropes (K).

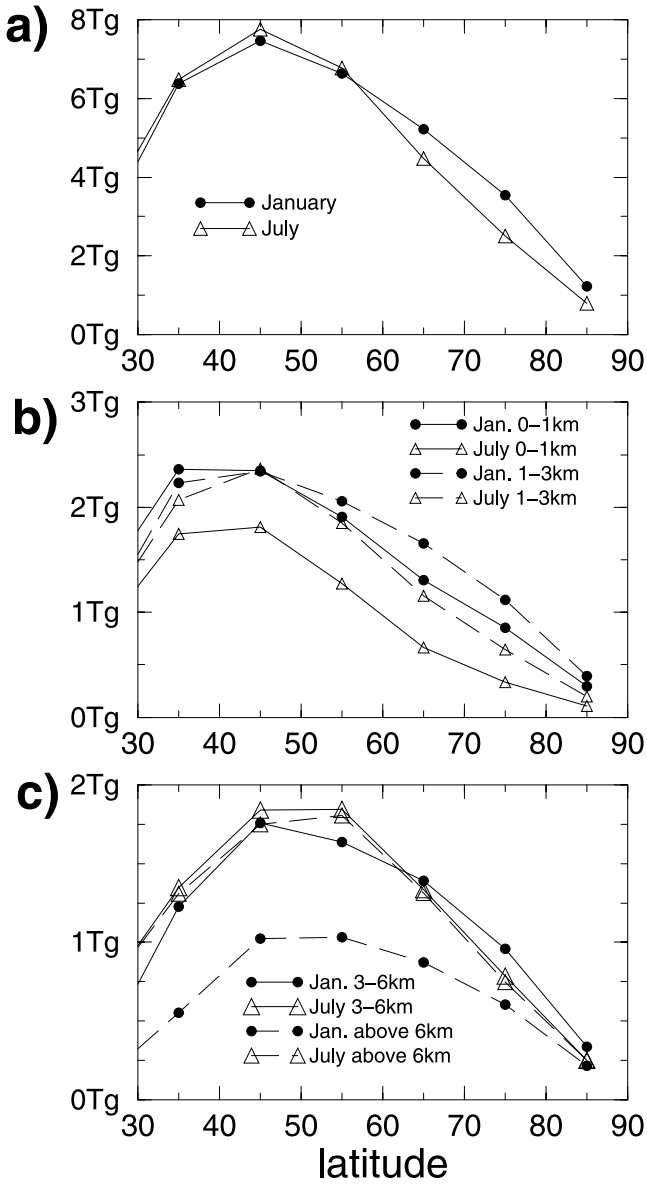

Figure 6. Zonally and vertically integrated mass of TRN averaged for the month of January and July. The vertical integral was calculated for (a) the whole troposphere, (b) from the surface to 1 km and 1 km to 3 km, (c) from 3 km to 6 km and from 6 km to the top of the model.

results of *Lamarque and Hess* [2003]. The prevailing circulation moves these emissions south, away from the Arctic. The Siberian emissions despite their small magnitude (only 7% of the total source), contribute more than 20% to the budget of TRN in the lower Arctic. They are ideally located on the pathway of transport to the Arctic. Emissions north of 45°N contribute over 50% to the concentration of TRN in the high latitude lower troposphere, but contribute less than 50% above 5 km.

[27] A plot analogous to Figure 10, but for TR7 is shown in Figure 12. Compared with TRN, emissions of TR7 north of 45°N contribute more to the tracer budget of the lower Arctic troposphere, but contribute less aloft. Similarly, the North American emissions of TR7 contribute more to the upper Arctic troposphere than those of TRN, but have less impact on the lower Arctic troposphere. This latter suggests relatively rapid transport along two primary transport pathways: the pathway from the North American emission region to the mid- and upper troposphere and from Eurasia to the lower Arctic troposphere. By contrast, the transport of North American emissions to the lower Arctic troposphere, or Eurasian emissions to the upper Arctic troposphere is slow (for an explanation see section 4). The Siberian sources of TR7, due to their proximity to the Arctic, play a particularly significant role (20–40%) in the lower Arctic.

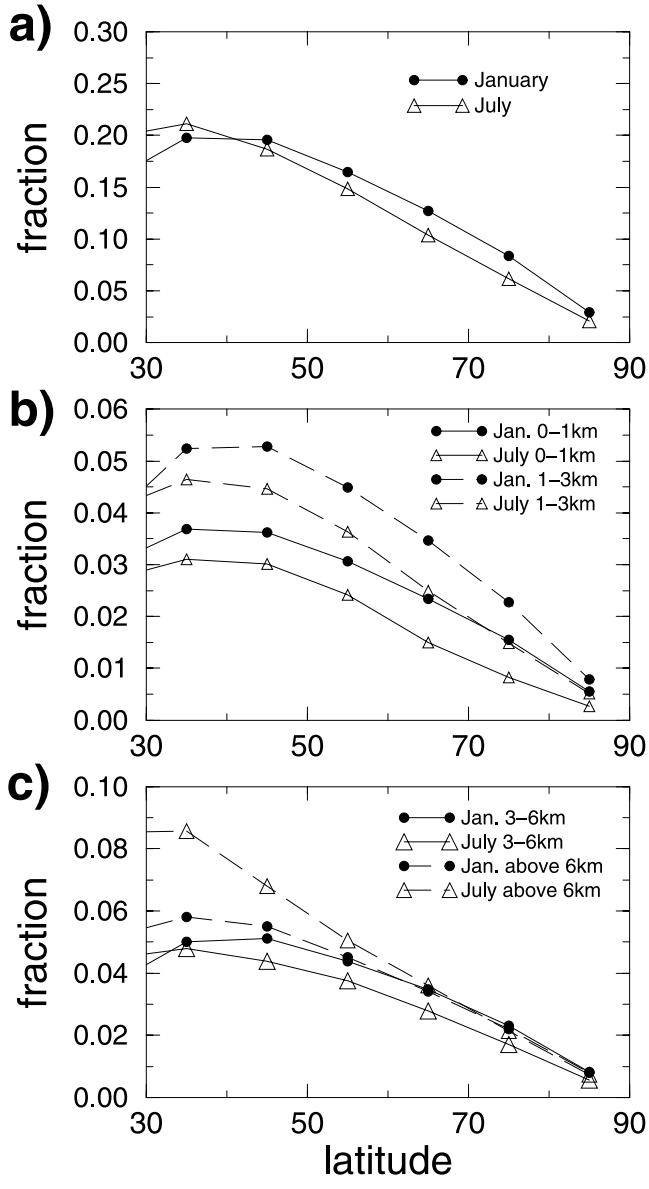

Figure 7. Zonally and vertically integrated mass of normalized CO averaged for the month of January and July. To account for the decrease in summer concentrations, the mass of CO for each month was normalized by the total mass of CO in the model during the given month. The vertical integral was calculated for (a) the whole troposphere, (b) from the surface to 1 km and 1 km to 3 km, (c) from 3 km to 6 km and from 6 km to the top of the model.

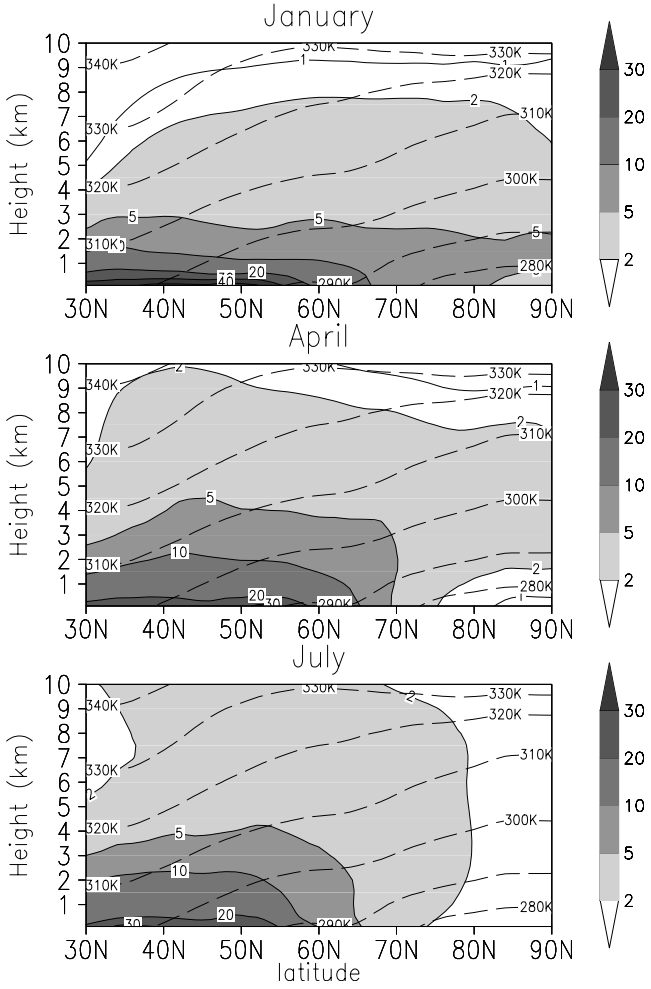

Figure 8. Monthly and zonally averaged mixing ratios of TR7 for January, April, and July in ppbv (solid lines, shaded above 2 ppbv). The dashed lines indicate the monthly and zonally averaged isentropes (K).

[28] The plots above represent zonal averages. Figure 13 shows TR7 averaged only over those longitudes in which TOPSE measurements took place (105W–60W). One of the most striking features of Figure 13 is the strong transport barrier separating North American and European emissions between 50°N and 60°N. This barrier extends from the surface through the mid-troposphere. In the short term the North American influence is largely confined south of this barrier, the European influence to the north. This barrier corresponds roughly to the location of the Arctic front during winter. Despite their large geographical distance from the Canadian Arctic, the European emissions of TR7 make the largest contribution to the near surface pollution there. Note that this analysis is based on monthly means. The contribution of a given emission region during a specific transport event can naturally be much higher.

[29] The results above apply to the year 2000. While it is beyond the scope of this paper to address interannual variability the results presented here should be generally applicable, at least in a qualitative sense. First, these results are supported by the numerous studies connected with Arctic haze. Second, many of the features can be explained through an analysis of isentropic transport (see section 4) valid in any given year. The interannual variability in CO due to transport is addressed by *Allen et al.* [1996].

3.2.2.2. Summer Case

[30] The greater vertical mixing rates during July (section 3.2.1) imply the emission contributions will not display the large vertical gradients found during the winter months (Figure 14). In July, the European emissions, due to their northerly location are the main contributor to TR7 throughout the depth of the troposphere north of 50°N. Thus, during the summer months, as distinct from the winter months, the European emissions are mixed upwards as efficiently as the North American emissions. North American emissions contribute somewhat more to the lower Arctic troposphere (10–20%) in July than in January, but much less to the upper troposphere (20–30%). Similarly the SE Asian emissions contribute less to the upper Arctic troposphere (10%), as the tracers emitted north of 45°N dominate the summertime budget there. In the TOPSE region during summer there is still a transport barrier separating North American and European emissions (not shown) on short timescales, as

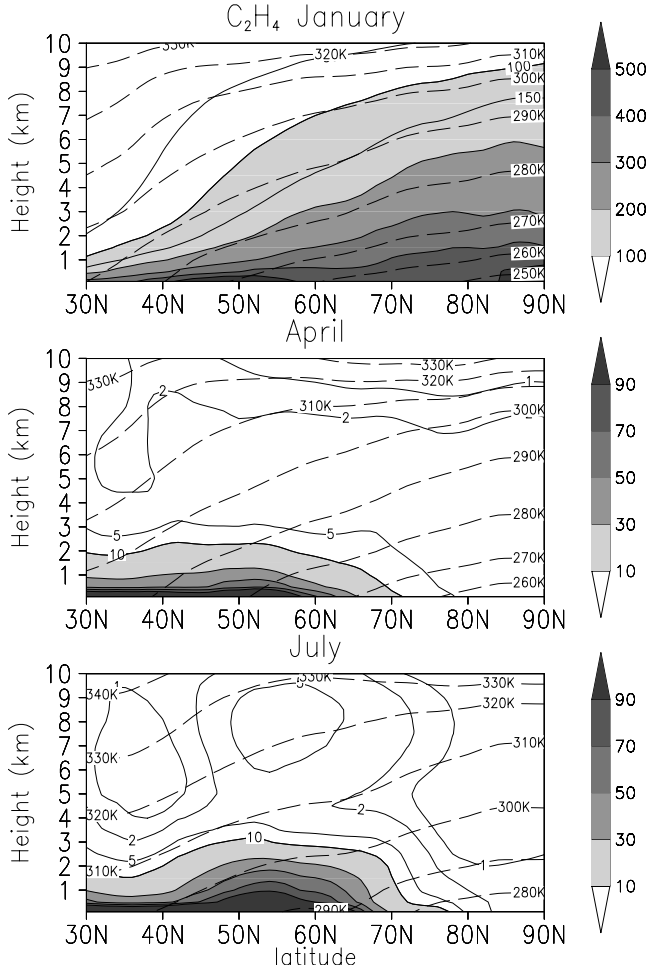

Figure 9. Monthly and zonally averaged mixing ratios of modeled C_2H_4 for January, April, and July in pptv (solid lines and shaded areas). The dashed lines indicate the monthly and zonally averaged isentropes (K).

Table 1. Fractional Contribution of Regional Sources to the Overall Tracer Emissions (First Column) and Contributions of the Regional Sources Binned by Latitude to the Overall Source (Remaining Columns)[a]

	% of Total Source	South of 30N % of total	30N–40N % of total	40N–50N % of total	50N–60N % of total	60N–70N % of total	70N–80N % of total	80N–90N % of total
All regions	100	16.6	36.5	27.3	18.2	1.4	0.01	NE
North America	24.9	1.4	15.5	7.5	0.4	0.02	0.0006	NE
Eurasia W of 40E (Europe)	30.4	NE	2.8	13.9	13.0	0.8	0.0009	NE
Eurasia S of 45, E of 40E	32.6	12.8	15.9	4.0	NE	NE	NE	NE
Eurasia N of 45, E of 40E	7.2	NE	NE	1.9	4.8	0.5	0.004	NE
All sources north of 45N	33.7	NE	NE	14.2	18.2	1.4	0.01	NE

[a]NE, No Emissions for a given latitude band.

was the case during winter (Figure 13), but during summer the barrier is located further north (between 60° and 70°N).

4. Interpretation of the Seasonal and Regional Transport Differences From an Isentropic Perspective

[31] Many of the seasonal transport changes during the TOPSE campaign can be partially attributed to seasonal changes in large-scale meteorological weather regimes as shown by e.g., *Barrie* [1986]. However, the description of the mean large scale meteorology says relatively little about seasonal differences in the vertical structure of transport. The isentropic perspective addresses this issue. Below, we outline how the isentropic perspective is applied to transport considerations, describe regional and seasonal differences in isentropic transport, and discuss how these relate to the regional and seasonal differences in heating and cooling rates.

4.1. Isentropic Perspective

[32] The isentropic perspective has been previously applied to tropospheric transport into the Arctic [e.g., *Carlson*, 1981; *Iversen*, 1984; *Raatz*, 1991]. It is based on the principle that in the absence of diabatic heating or cooling (by latent heat release, sensible heating, or the absorption and emission of long and short wave radiation) a parcel will simply be transported along constant isentropic surfaces, not across them. Throughout most of the free troposphere slow radiational cooling prevails and parcels are slowly transported to lower potential temperatures. These widespread regions of slow cooling are balanced by limited regions of strong diabatic heating (leading to rapid upwards transport across isentropic surfaces) corresponding to regions with precipitation (i.e., heating due to latent heat release), or to locations where the earth's surface provides a large sensible heat source (i.e., in the boundary layer). Note however, that during wintertime, the cold continental boundary layer can also provide a strong cooling mechanism (see section 4.4). The confinement of strong cross-isentropic transport to limited regions makes the isentropic perspective particularly useful.

[33] When diabatic heating (or cooling) and chemistry are slow compared with transport timescales, mixing will homogenize tracer concentrations along isentropic surfaces. As a result the isolines of the tracer and those of the isentropic surfaces will be in close correspondence. Figures 4 and 5 (despite the averaging that encompasses various meteorological conditions) demonstrates this correspondence for TRN and CO in the free troposphere during January, and to some extent April. C_2H_4 only shows this correspondence in January when its lifetime is relatively long. The isentropic mixing timescale is evidently never fast enough to mix TR7 along isentropic surfaces (Figure 8). Due to the characteristic slope of isentropes in the troposphere (Figure 4) the more southerly emissions are more easily transported (without significant cooling or heating) into the upper arctic troposphere than those to the north. This partially explains the greater tracer burden in the upper arctic troposphere from the more southerly emission sources (see Figure 10).

4.2. Seasonal Transport Differences From an Isentropic Perspective

[34] Figure 4 implies large seasonal differences in the location and strength of diabatic heating (cooling) between winter and summer. 1) Strong diabatic cooling must occur during transport into the lower Arctic troposphere during the winter months. During winter the highest concentrations of TRN in the Arctic latitudes occur near the surface and therefore at potential temperatures consistently lower than the primary sources of emission. 2) The cooling associated with transport to the Arctic is considerably weaker during summer than during the winter months. During summer the vertical gradient of TRN over the lower Arctic is reversed (i.e., TRN increases with height, see Figure 4) and the highest concentrations of TRN occur in the mid-troposphere at, or near, the potential temperature of its primary emission source. 3) During July there is an increase in the diabatic heating due to convection and boundary layer heating in the midlatitudes. The vertical lofting of tracers in the midlatitudes increases compared with earlier in the year. To examine the points above in more detail, in the following analysis we label the distribution of the non-reactive tracer (TRN) by the potential temperature of its emissions. This labeling is done in 10K intervals, so, for example, if the potential temperature at the surface is 275K, the tracer labeled between 270 and 280K is emitted. Since the surface temperature changes every 3 hours in HANK, the emitted species are also updated with this frequency. Recall, that if the diabatic heating or cooling rates were zero, the labeled tracers would be confined to potential temperatures at which they were emitted, but since these rates are non-zero, the tracers are redistributed to other potential temperatures. Figure 15 shows the zonally and monthly averaged mixing ratio of TRN labeled by its predominant emission temperature in winter and summer: 270–280K in winter and 290–300K in summer. TRN appears to have an elevated source in summer, but not in winter. The emissions of TRN are mostly over land, and therefore within any particular

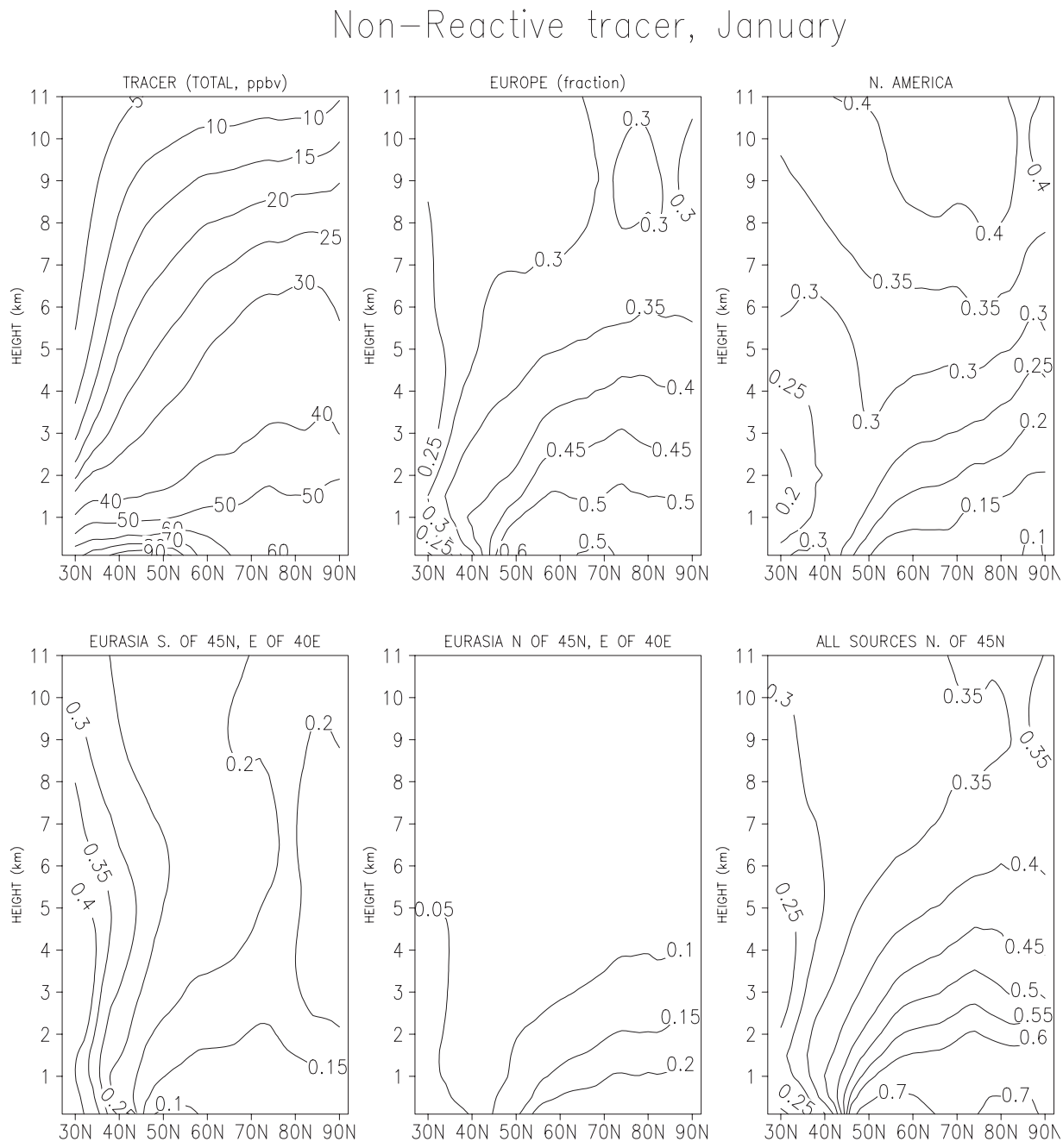

Figure 10. Monthly and zonally averaged concentrations of TRN for January (in ppbv) and the contribution from the 5 main emissions regions (shown as fraction of the total, between 0 and 1).

latitude band the emissions tend to be at relatively warm temperatures during summer (the oceans, without significant emissions are at relatively lower temperatures), but at relatively cold temperatures during winter. As a consequence, from an isentropic perspective, the highest concentrations are at the surface during winter, but are elevated during summer.

[35] Figure 15 shows that for both winter and summer, within two months of integration, a large fraction of TRN is redistributed to potential temperatures other than those at which it was emitted. During winter, however, significantly more of the emitted species sinks to colder temperatures. The difference in diabatic cooling is particularly strong in the high latitudes as shown quantitatively in Table 2. During winter north of 60°N almost 40% of the tracer sinks diabatically below the original emission bin compared with only 16% during summer. Heating to higher potential temperatures is significant during both seasons but is more pronounced in summer as indicated by the bowed isolines in Figure 15 and data in Table 2.

4.3. Transport From Eurasia and North America Into the Arctic From an Isentropic Perspective

[36] The isentropic perspective further accentuates the differences in the transport pathways of North American and European emissions. 1) The main Eurasian sources are

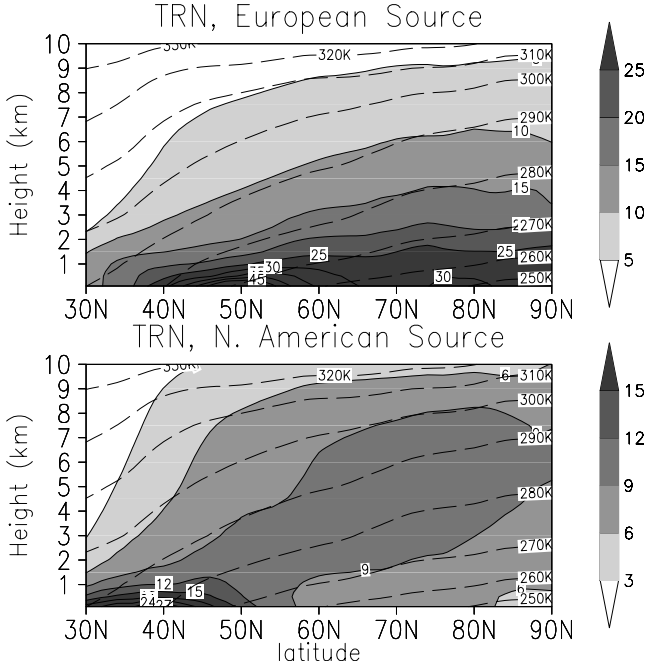

Figure 11. Monthly and zonally averaged mixing ratios of TRN emitted over Europe and over North America for January, in ppbv. The dashed lines indicate the monthly and zonally averaged isentropes (K).

located further north than the North American sources (often north of the Arctic front) and at lower potential temperatures (see Table 3). This enables them to be transported northward with a minimum of additional cooling [see, e.g., *Raatz*, 1991]. 2) The northern Eurasian emissions experience significantly stronger diabatic cooling than the North American emissions. We show this latter point in greater detail below. We concentrate on the winter months when the differences between these two emission sources are most pronounced.

[37] To quantify the amount of diabatic cooling during transport into the Arctic we repeat the simulation with the diagnostic tracer TR7 labeled by both the potential temperature of its emissions and its region of origin (either Europe or North America). We use the tracer with the seven day lifetime (TR7) as it allows an examination of transport pathways immediately downwind from its emission source. In Figure 16 (compare with Figure 11) we only show the results for the largest emission bin (see Table 3) for the Eurasian and North America emissions for January: the 270–280K temperature bin for Europe and 280–290K bin for North America. Clearly there is a qualitative difference between the transport of the North American and European emissions into the high latitudes. In the case of North American emissions the pollution is largely transported to higher potential temperatures, while the pollutants from Europe exhibit significant sinking. The percentage of tracer mass north of 60°N within the original temperature bin, at temperatures above this bin, and at temperatures below it, is given in Table 4. Significantly more of the European tracer sinks below the 270K isotherm (almost 40%) than is lifted above the 280K isotherm (21%). The opposite is true for the North American tracer: less of this tracer sinks to a lower temperature bin than is lifted to a higher temperature bin (30% vs. 41%). The difference is even larger for the North American tracer emitted between 270 and 280K (its emissions, as shown in Table 3, are comparable to the emissions between 280 and 290K): only 14% sinks to a lower temperature bin and over 60% rises to a higher potential temperature bin.

4.4. Discussion of Seasonal and Regional Diabatic Heating Rates and Their Relation to Transport

[38] Figure 17, which depicts the near surface net diabatic rates from the NCEP analysis for January 2000, shows that boundary layer air experiences strong cooling over much of Eurasia and North America. The cooling is of the order of several degrees per day and is predominantly due to contact with the cold and mostly snow covered surface. Figure 18a (open circles) shows the vertical profile of the NCEP diabatic heating rates averaged for January over a region downwind from the major European emissions (from 15°E to 90°E and 50°N to 70°N). The averaged vertical profile indicates that strong cooling is concentrated in the boundary layer. This strong boundary layer cooling provides an efficient mechanism whereby the European emissions can be transported to the lower Arctic troposphere given the appropriate large scale transport. Above the boundary layer the cooling rates are on the order of 1K/day, as expected in the free troposphere due to radiational cooling.

[39] Regions with strong surface cooling are also characterized by persistent temperature inversions (e.g., as discussed by *Raatz* [1991]). In wintertime strong surface inversions are common over the northern parts of Eurasia and the high Arctic (see Figure 18b). Boundary layer inversions are important for transport to the Arctic: they limit the mixing of pollutants into the free troposphere and thereby expose the pollutants to periods of prolonged strong surface cooling. This boundary layer trapping of pollutants over northern Eurasia is illustrated in the vertical profile of CO (Figure 18c). Since this region is directly downwind of the major European emissions, the emitted pollutants are expected to undergo large diabatic cooling as they are transported eastward over the cold snow covered surface of north-eastern Europe and Siberia under a strong temperature inversion.

[40] The above conditions are not met for North American pollution, which because of the predominant track of weather systems is largely swept off the North American continent and over the North Atlantic. Figure 17, and the regionally averaged heating profile in Figure 18a (averaged downwind from the North American emissions) indicates considerable heating in the North Atlantic boundary layer during the winter months. The strong boundary layer heating is primarily due to sensible heating, heating which occurs during the winter months as cold continental air is advected over the relatively warm ocean off the North American continent. The Gulf Stream in particular accentuates this heating. Figure 18b shows no indication of an inversion layer over the North Atlantic. Figure 18c shows CO is not trapped in the oceanic boundary layer (as it is in the continental boundary layer), reflecting rapid boundary layer mixing and transport of pollutants to the free troposphere. Above the boundary layer, Figure 18a indicates

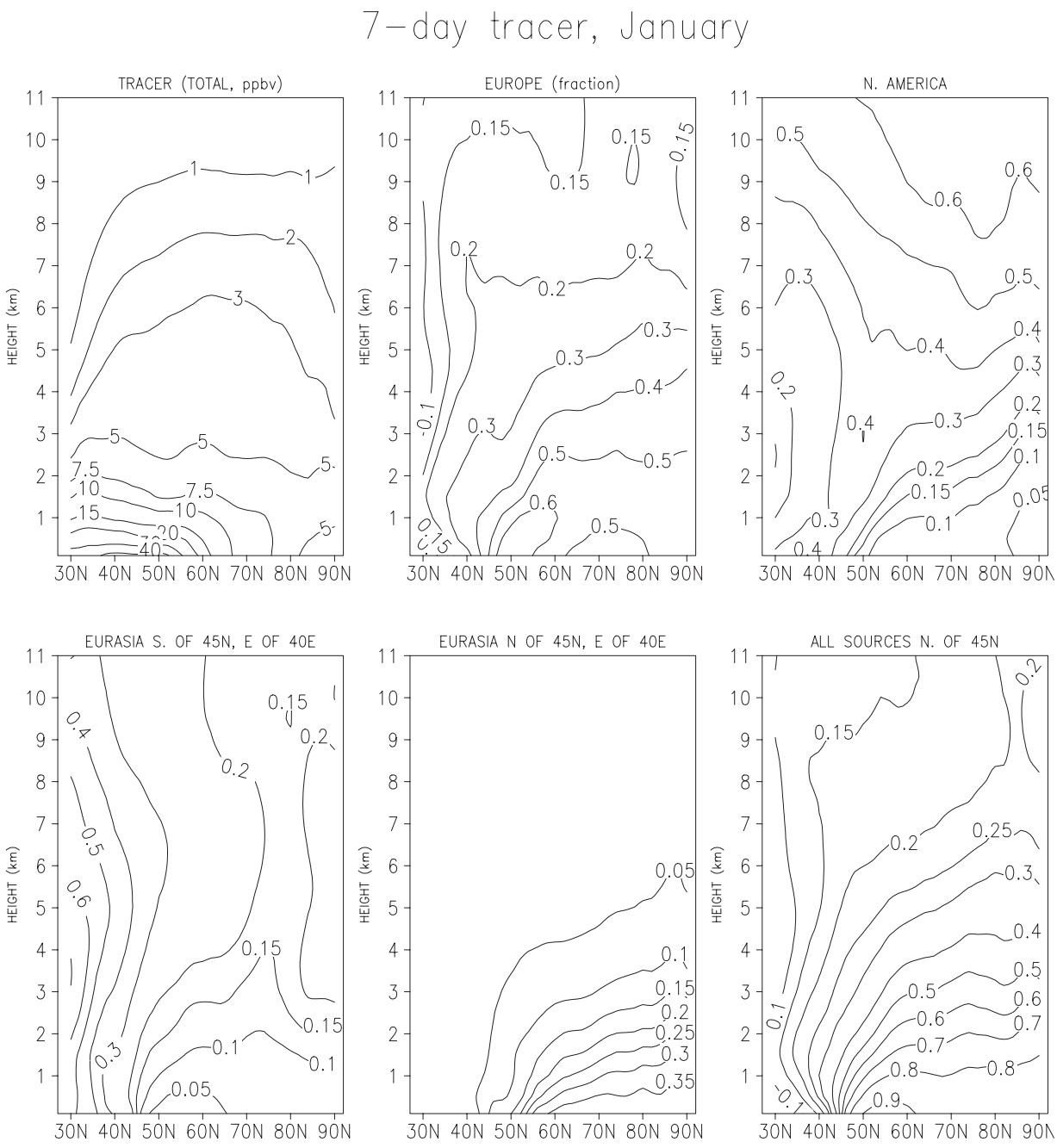

Figure 12. Monthly and zonally averaged concentrations of TR7 for January (in ppbv) and the contribution from the 5 main emissions regions (shown as fraction of the total, between 0 and 1).

weak heating extending upwards throughout most of the depth of the free troposphere. This heating is due to frequent precipitation within the strong storm track located just off the east coast of the U.S [e.g., *Hoskins and Valdes*, 1990].

[41] The summertime export of North American pollutants may occur somewhat differently, with the land surface generally warmer than that of the ocean. *Angevine et al.* [1996a, 1996b] discuss different scenarios for the transport of North American pollutants over the ocean during summer. The emissions can either be trapped in the oceanic boundary layer, resulting in a stable layer of high pollutant concentrations over the ocean, or they can be transported over the boundary layer, resulting in a relatively clean maritime layer below.

5. Conclusions

[42] In this study we use a regional chemical transport model to examine seasonal differences in the transport of pollution in the mid and high latitudes of the Northern Hemisphere. After demonstrating that the model qualitatively reproduces the seasonality of CO and a number of hydrocarbons measured during the TOPSE campaign, we analyze the differences in model transport during different

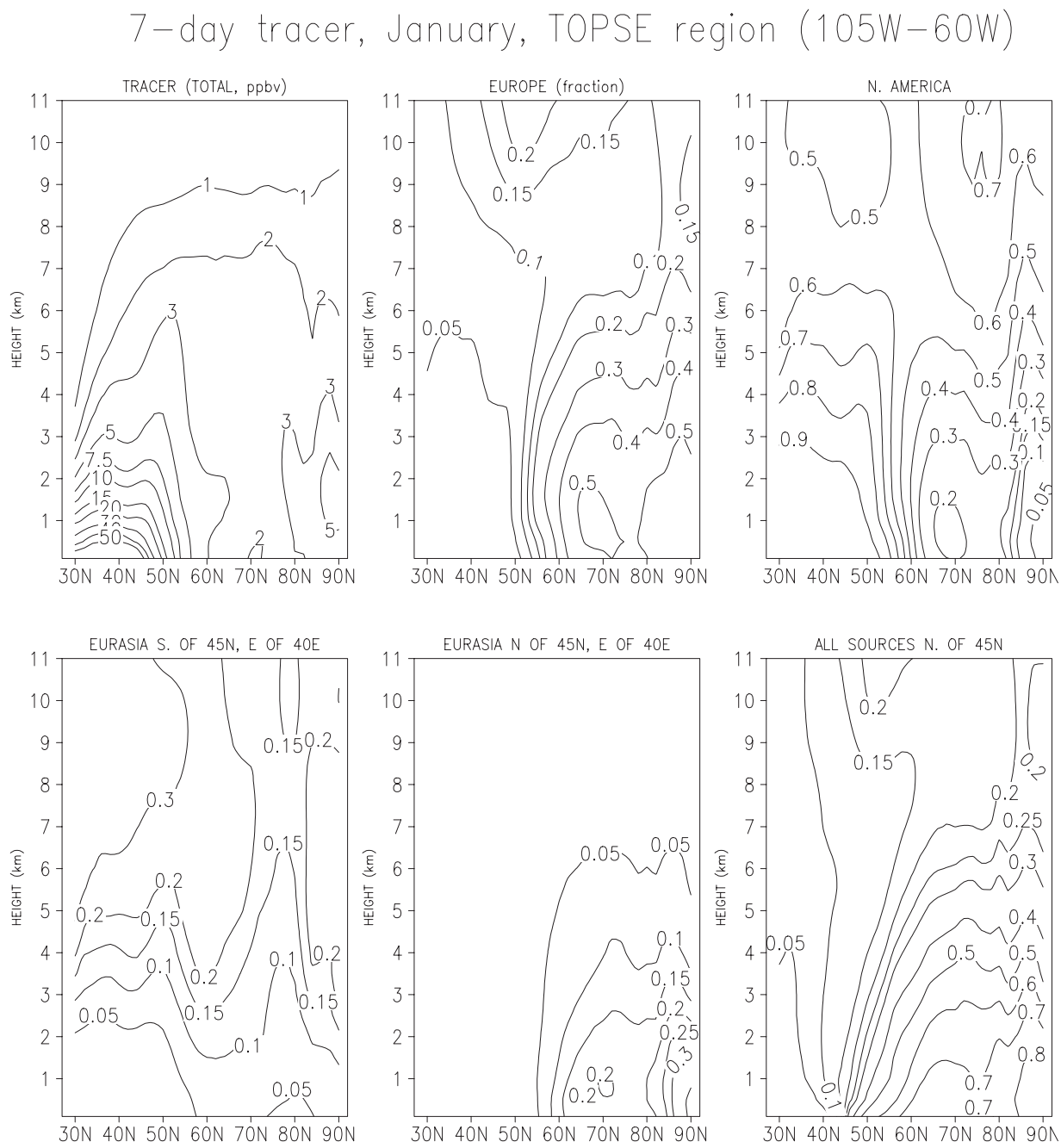

Figure 13. As in Figure 12 but the average calculated only over the TOPSE region (105W−60W).

seasons and from different emission regions. To separate the effect of chemistry from that of transport we conducted model simulations with diagnostic tracers which were either non-reactive or had a constant decay lifetime of 7 days. Results show that due to transport differences alone, there is a large seasonal cycle in the concentrations of the diagnostic tracers in the high latitudes. The largest seasonal difference is simulated within the lowest few hundred millibars above the arctic surface. This region has maximum concentrations in winter in agreement with results from earlier studies of the Arctic Haze. In the middle and upper troposphere, on the other hand, higher concentrations are simulated during summer. The distributions of CO and the analyzed HCs, despite the masking due to changing oxidant concentration, show transport related features similar to those of the diagnostic tracers.

[43] This paper quantifies the contributions of 5 emission regions to the concentrations of the non-reactive and 7-day tracer in the mid and high latitudes of the Northern Hemisphere and over the particular sector corresponding to the TOPSE measurements. During winter the European source is clearly dominant in the lower half of the Arctic. This result is consistent with studies of the anthropogenic trace elements in Arctic Haze [e.g., *Lowenthal and Rahn*, 1985], studies of the meteorology over the region [e.g., *Raatz*, 1991], and previous modeling studies [*Levy and Moxim*, 1989]. Budgets for the longitudes sampled during the TOPSE campaign (105°W to 60°W) show a strong mixing barrier in the lower

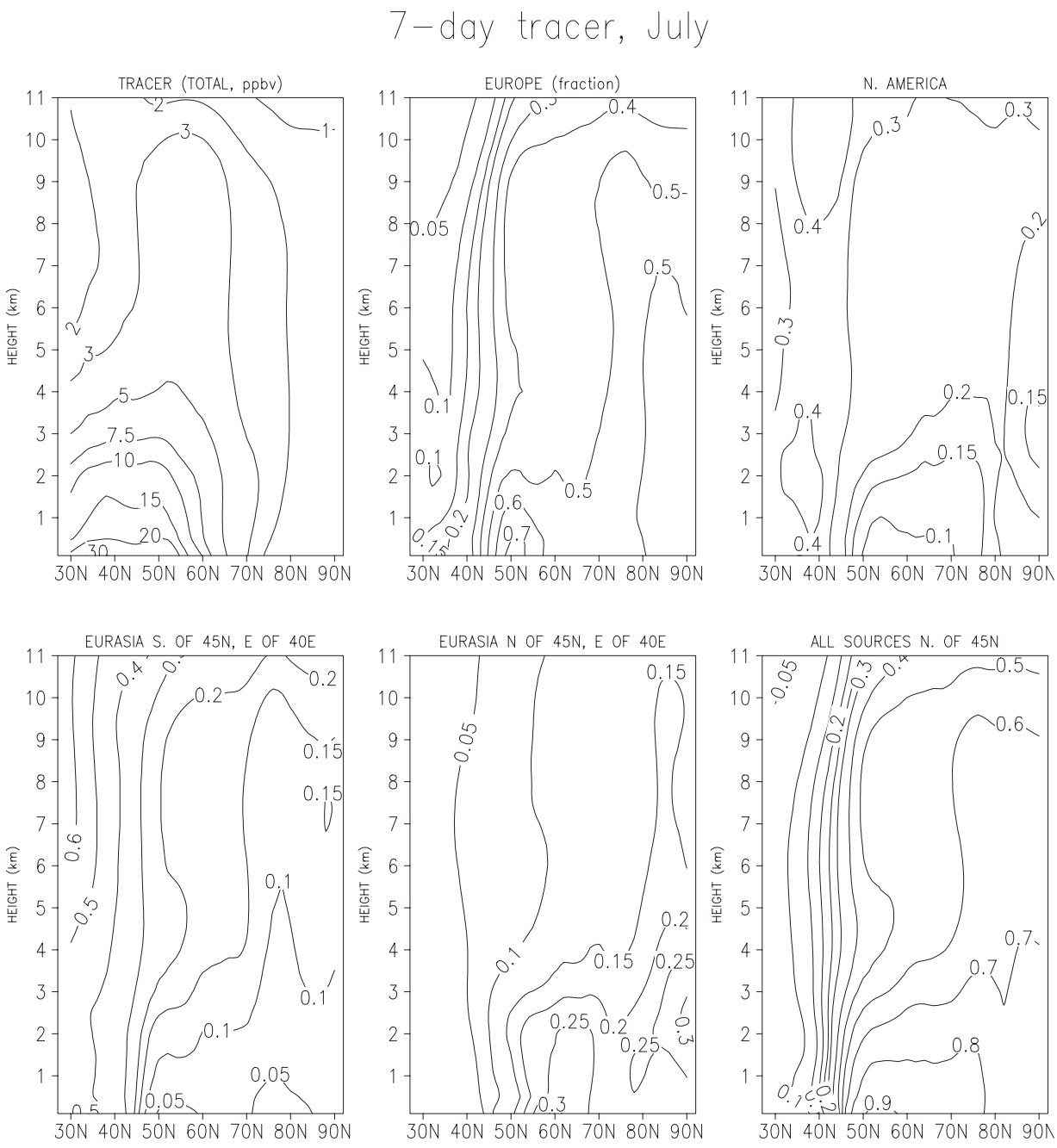

Figure 14. As in Figure 12 but for July.

troposphere near 60°N between the short-lived species (TR7) emitted in North America and Europe. South of this line, and particularly below 4 km, the simulations suggest that the TOPSE measurements of short-lived species were predominantly of North American origin. North of this barrier the contribution of the North American emissions is generally small near the surface, but increases with height. During summer the pollution is mixed vertically to a greater extent and the strong mixing barrier over North America moves considerably north, presumably following the location of the Arctic front. The relative contributions deduced here for TR7 and TRN are likely to change for species with different lifetimes, for species with different emission patterns, and for species affected by wet removal and presence of secondary sources (e.g. Arctic Haze).

[44] Examining transport from an isentropic perspective provides a clear and coherent picture of differences in transport between different emission regions and different seasons. It can explain many aspects of the tracer distributions examined above. In winter, during meteorological conditions which favor the northward transport of the pollution accumulated over northern Eurasia, diabatic cooling, reinforced by the presence of strong inversions, allows the polluted airmass to be transported to the lower Arctic troposphere. In summer, on the other hand, there is no efficient cooling mechanism which can rapidly cool polluted plumes to the potential temperatures characteristic of the lower summertime Arctic. On the contrary, the Eurasian boundary layer experiences weak heating on average, and due to relatively high surface temperatures is less stable. As

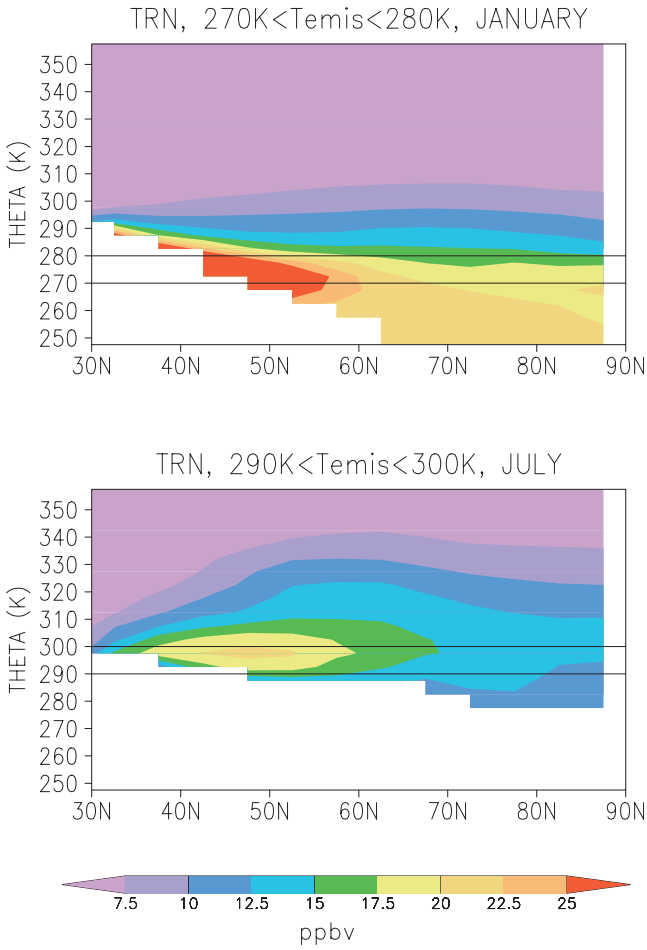

Figure 15. Monthly and zonally averaged concentration of TRN interpolated to surfaces of constant potential temperatures for (a) the main emission temperature in January: 270–280K and (b) the main emission temperature in July: 290–300K. More detailed description in the text. Due to surface temperature variations in longitude, all longitudinal points on a particular potential temperature surface may not be defined. A zonal average is taken only if the value at a given level is defined for at least 25% of all grids at that latitude for all time steps during the month, otherwise the point is left blank.

a result there are fewer temperature inversions and pollutants are mixed more rapidly into the free troposphere. As a consequence, emissions are transported to the Arctic at higher altitudes in the summer, leading to a positive tracer gradient with height in the lower Arctic troposphere. During winter, it is the European emissions that predominantly influence the lower arctic atmosphere while the N. American emissions become more important up high. In contrast to the strong cooling mechanism that exists for European emissions as they are transported northward, North American pollutants are swept off the continent and are transported over the relatively warm Atlantic ocean where they experience strong vertical mixing. In addition, a prominent storm track located off the east coast of the U.S. provides a further lifting mechanism.

Appendix

[45] The goal of this appendix is to describe the major differences between the model used in this study and its earlier version described in *Hess et al.* [2000]. Most of the changes were introduced to make the model suitable for the high latitudes - the model used in *Hess et al.* [2000] was used to simulate chemistry over the subtropical Pacific. The changes are itemized below.

1. Daily sea-ice was included in MM5 based on satellite observations archived at the National Snow And Ice Data Center [*Cavalieri et al.*, 2002; *Comiso*, 2002] by changing the surface type from water to ice when the observed ice coverage exceeded 50%. This modification allowed the surface temperatures to reach sub-zero values and allowed differences in transport to be simulated over water and ice surfaces.

2. A moisture scheme allowing for the formation of snow, ice and supercooled water was used in the MM5 [*Grell*, 1993a].

3. The parameterization of wet removal has been expanded to include the removal of species frozen in ice and the removal of nitric acid that deposits on the surface of ice (through snow fallout). As in *Hess et al.* [2000] the *Giorgi and Chameides* [1985] scheme is used. However, while previously the chemical concentrations were simply partitioned between the gaseous and aqueous phase [*Hess et al.*, 2000], here the species is partitioned between the aqueous, ice and gas phase. The removal of a species due to wet deposition (R_{wet}) can be written as:

$$R_{wet} = \frac{\chi}{10^{-6} \cdot (L_{aq} + L_{ice}) + 1/(HRT)} \cdot (P_{aq} + P_{ice})$$

where L_{aq} is the liquid content of a cloud including rainwater and cloud water, L_{ice} is the ice content of a cloud

Table 2. Distribution of TRN Labeled by Emission Potential Temperature Integrated for Latitudes North of 60°N for January and July[a]

Region of Emission of TRN	Month	Tracer Type (Emitted for Θ Between)	Total Mass of the Tracer (Tg) North of 60°N	% of the Tracer in the Original Potential Temperature Layer	% of the Tracer Below the Layer (Cooling)	% of the Tracer Above the Layer (Heating)
All sources	January	270–280K	4.10	26.4	38.6	35.0
All sources	January	sum over all temperature bins	10.01	24.9	41.0	34.1
All sources	July	290–300K	3.58	26.5	16.3	57.2
All sources	July	sum over all temperature bins	7.80	23.9	20.0	56.1

[a]The tracer can be either in, below, or above its emission potential temperature bin. The values are given for the main emission temperature bins (270–280K in winter and 290–300K in summer) and summed over all temperature bins. The given values are monthly averages.

Table 3. Total Emissions of TRN and TR7 Integrated for December and January for Five Potential Temperature Emission Bins (in Tg)

Region of Emissions	Θ_{emis} < 260K	260K < Θ_{emis} < 270K	270K < Θ_{emis} < 280K	280K < Θ_{emis} < 290K	290K < Θ_{emis}
North America	0.60	3.29	6.39	7.16	2.15
Eurasia W of 40E (Europe)	0.28	3.18	13.65	5.10	0.05
Eurasia S of 45, E of 40E	0.52	2.39	6.60	10.02	8.52
Eurasia N of 45, E of 40E	1.57	2.43	1.27	0.02	0.00
All sources north of 45N	2.01	5.83	13.93	2.92	0.00

including ice and snow, H is Henry's Law constant, R is the gas constant, T the temperature, χ the species concentration, and P_{aq} and P_{ice} the removal efficiency (kg/m^3/sec). Here we assume that a species is incorporated into liquid before it freezes into snow (or ice) and remains in the snow and ice after it freezes. The removal efficiency of rainwater is approximated as:

$$P_{aq} = \frac{q_{rain} \cdot \rho_{air} \cdot \delta_{cloud}}{\int_0^{Z_{top}} (q_{rain} + q_{snow}) \cdot \rho_{air} \cdot \delta_{cloud} dz} P_r$$

A similar equation applies for P_{ice}, with q_{rain} replaced by q_{snow}. Here ρ_{air} is the density of air, P_r is the precipitation rate (kg/m^2/sec) and q_{rain} and q_{snow} are the mixing ratio of rain and snow in a cloud (kg/kg). The δ_{cloud} parameter, defined to be 0.1 outside of a cloud and 1 within a cloud, is added to allow for higher scavenging of gases in-cloud than below-cloud. The denominator is integrated from the ground to the top of the cloud deck (Z_{top}).

In addition, the deposition of nitric acid on an ice surface was added to account for the suggested fast deposition of HNO_3 on ice [e.g., *Abbatt*, 1997; *Zondlo et al.*, 1997]. The number of molecules of HNO_3 removed per unit volume from the gas phase due to deposition on the surface of ice can be defined as: $\chi_{ice} = A_{ice} \cdot D$, where A_{ice} is the surface area of ice crystal per unit volume, and D is the number of sites at which HNO_3 can stick to the ice surface per cm^2. D is assumed here to be 2×10^{14} molecules/cm^2 (after *Abbatt* [1997]). Making the assumption that ice crystals are spherical, A_{ice} can be obtained from the empirical relationship between ice cross sectional area (S_{ice}) and ice water content (q_{ice}) which we derived by fitting data from the ARM campaign (*Heymsfield,* private communication, 2000) using the functional form from *Heymsfield and McFarquhar* [1996].

$$A_{ice} = 4 \cdot S_{ice} = 4 \cdot \left(50.4 \cdot (q_{ice})^{0.872}\right)$$

The amount of HNO_3 removed from a model layer by deposition onto ice is then assumed to be: $A_{ice} \cdot D \cdot \frac{P_{ice}}{(q_{ice}+q_{snow}) \cdot \rho_{air}}$,

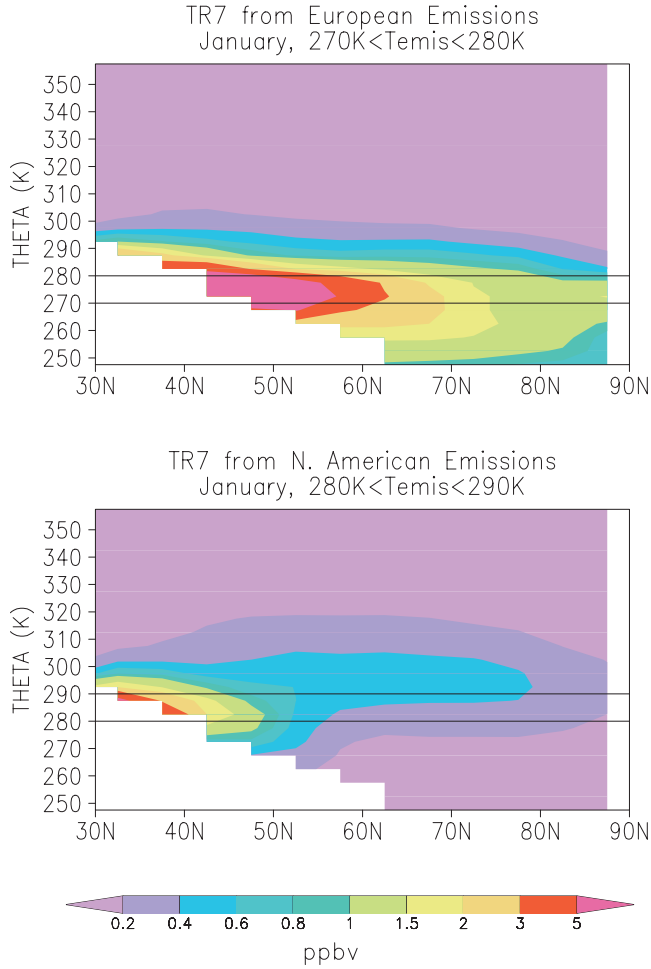

Figure 16. Monthly and zonally averaged concentration of TR7 in January interpolated to surfaces of constant potential temperatures for (a) the tracer emitted over Europe at potential temperature of 270–280K, and (b) the tracer emitted over N. America at potential temperature of 280–290K.

Table 4. Distribution of the TR7 Labeled by the Emission Potential Temperature and Region of Emission (Europe and North America) for January[a]

Region of Emissions of TR7	Month	Tracer Type (Emitted for Θ Between)	Total Mass of the Tracer (Tg) North of 60°N	% of the Tracer in the Original Potential Temperature Layer	% of the Tracer Below the Layer (Cooling)	% of the Tracer Above the Layer (Heating)
Europe	January	270–280K	0.29	39.7	39.6	20.7
Europe	January	Sum over all temperature bins	0.54	37.4	38.8	23.8
North America	January	280–290K	0.08	28.5	30.4	41.1
North America	January	270–280K	0.10	23.1	13.8	63.1
North America	January	Sum over all temperature bins	0.26	22.8	18.0	59.2

[a]The mass of the tracer is integrated only for latitudes north of 60°N.

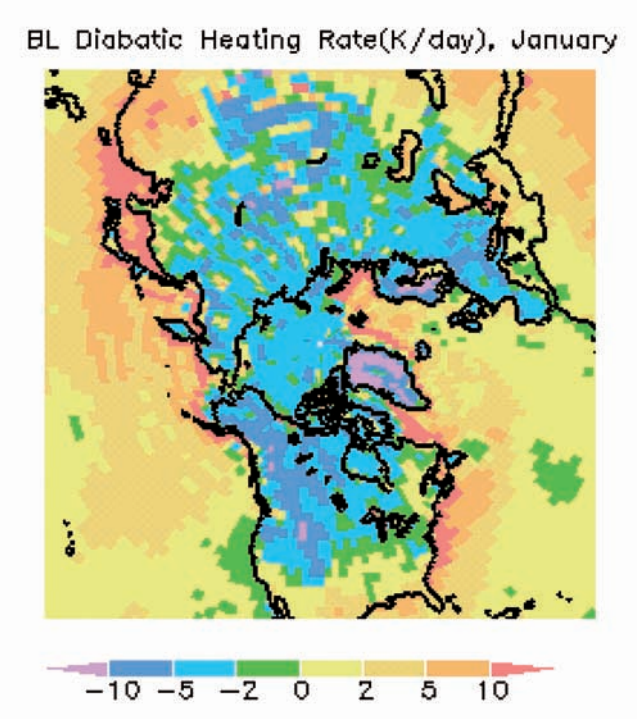

Figure 17. Near surface diabatic heating rate from the NCEP model averaged for January.

where the ratio estimates the rate of removal of snow from the layer (1/sec).

4. The reaction accounting for the heterogeneous removal of N_2O_5 on the surface of aerosols was added to the chemical mechanism. The rate of removal (in units of 1/sec) is given by: $\gamma \cdot S \cdot \sqrt{\frac{8kT}{\pi \cdot M/N_A}} \cdot 0.25$, where k is the Boltzmann's constant, γ is the reaction probability, S is the surface area of the aerosols per unit volume calculated from the equilibrium size distribution, T is temperature, M molecular weight of N_2O_5 and N_A is the Avogadro's number. The monthly averaged distribution of aerosol mixing ratio was taken from *Barth et al.* [2000]. The surface area of aerosols was calculated assuming a lognormal size distribution of dry aerosols with a mean radius of 0.05 μm and a standard deviation of 2. At a given relative humidity a new equilibrium size distribution was calculated using the method given in *Kiehl et al.* [2000] assuming the aerosol are composed of $(NH_4)_2SO_4$. We assumed efflorescence occurs at 35% relative humidity regardless of temperature. We used a temperature dependence of γ similar to that given in *Hallquist et al.* [2000]: $\gamma = \gamma_{300} + (\gamma_{200} - \gamma_{300}) * (300 - T)/100$, where γ_{300} and γ_{200} are rate coefficients at 300 and 200K, set respectively to 0.003 and 0.0185. These rates are significantly lower than those recommended by *Hallquist et al.* [2000], but the total removal rate is equal to the surface area times the reaction probability and the surface area is not well known. Lowering these rates was intended to increase NO_x in HANK to match the TOPSE measurements so as to simulate the correct ozone production rates. *Tie et al.* [2003] analyzes the sensitivity of the solution to this reaction.

5. A lightning source of NO_x was added based on the parameterization of *Price and Rind* [1992]. The lightning source of NO_x was distributed in the vertical according to the recommendations of *Pickering et al.* [1998].

6. Ozone was relaxed in the stratosphere above PV = 2 surface with a relaxation time of 5 days to values determined by the O_3/PV parameterization described in *Klonecki et al.* ("Analysis of the correlation between O_3 and potential vorticity in the lower stratosphere and possible applications", in preparation). The parameterization consists of quadratic fits of the ozonesonde data and matching PV values from NCEP analysis. The fits change monthly but a single fitting function is applied throughout the lower stratosphere for the whole model domain. The stratospheric values of HNO_3 were similarly relaxed based on the measured O_3/HNO_3 ratio from the TOPSE campaign.

7. The chemistry mechanism for the TOPSE experiments was updated from that given in *Hess et al.* [2000]. The new mechanism can be found at http://acd.ucar.edu/models/HANK. A summary of the changes is given here. The reaction rates have been brought up-to-date with those in *Sander et al.* [2000]. The reaction rates of many of the peroxy-peroxy radical reactions, and the peroxy radical reaction rates with NO, including the formation of PAN and MPAN were updated following the recommendations given in *Tyndall et al.* [2001], *Villenave and Lesclaux* [1996], *Carter et al.* [1996], *Tuazon and Atkinson* [1990], *Orlando et al.* [1999], and *Eberhard and Howard* [1997]. The oxidation scheme of C_2H_4 was expanded following the mechanism from *Niki et al.* [1981] and updated from laboratory measurements by *Orlando et al.* [1998]. The oxidation mechanism for acetone was updated [*Wollenhaupt et al.*, 2000, and *Orlando et al.*, 2000]. The ozonolysis of C_2H_4 and C_3H_6 were updated following *Atkinson et al.* [1997], while the oxidation mechanism of isoprene, MVK (methyl vinyl ketone) and MACR (methacrolein) have been updated following *Carter and Atkinson* [1996] and *Gierczak et al.* [1997]. Additional updates include: the oxidation rate of isoprene by OH and O_3 [*Atkinson et al.*, 1997]; the reaction rates of alpha-pinene with OH and O_3; the glyoxal photolysis rate and products following *Zhu et al.* [1996]; the reaction rate of OH and HNO_3 following *Brown et al.* [1999]; the products of the reaction of NO_3 with HO_2; the reaction rates of NO_3 with C_3H_6 and ozone with C_3H_6 [*Atkinson et al.*, 1997]; the reaction rate of the lumped organic nitrate with OH following *Brasseur et al.* [1998], and the rate constant for the reaction between H_2O and N_2O_5 has been decreased following the recommendation of *Wahner et al.* [1998]. In addition, CH_3OH has been added to the oxidation mechanism for methane. To prevent an excessive build-up of the lumped nitrate species its washout rate was arbitrarily set to four times that of HNO_3.

8. The emissions used in the model have been updated based on the 1° × 1° inventory developed by C. Granier and M. Schultz (http://acd.ucar.edu/models/MOZART/emissions/emissions.html and published in *Horowitz et al.* ("A global simulation of tropospheric ozone and related tracers: Description and evaluation of MOZART, version 2", manuscript submitted to *Journal of Geophysical Research*, 2003).

9. The MM5 simulations which provided the input fields to HANK consisted of overlapping 30 hour segments. In each of these simulations the initial six hours were discarded, allowing for model spin-up. The winds and other dynamical parameters calculated for the last 24 hours were then used to transport species in HANK. The NCEP

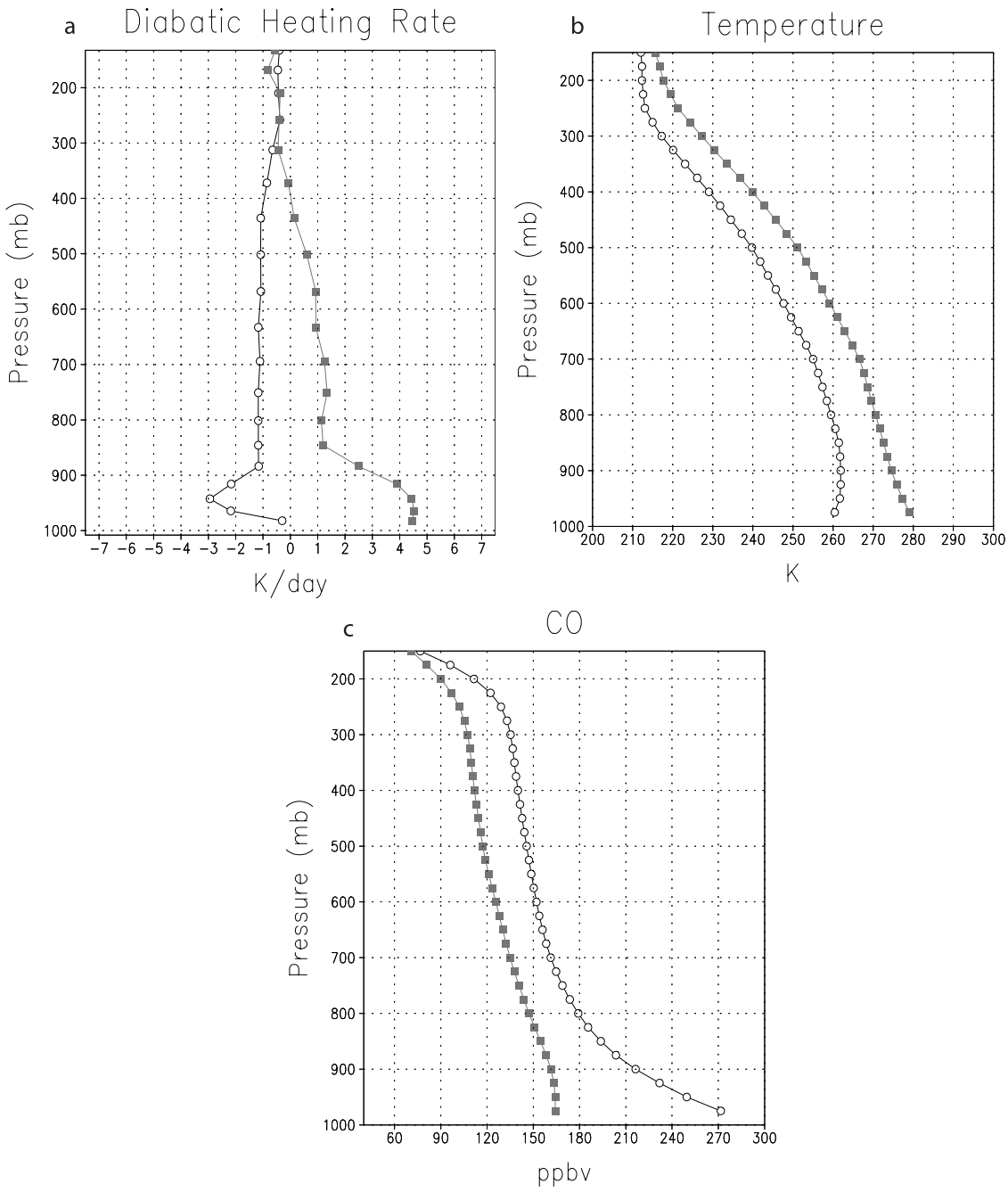

Figure 18. Vertical profile for (a) the diabatic heating rate from the NCEP model (K/day), (b) temperature profile (K) from the MM5/HANK model and (c) CO profile (ppbv) from the HANK model. The profiles were averaged for January. The open circles represent an average over a region in Eurasia (15E–90E, 45N–70N) and closed squares a region over the North Atlantic (70W–50W, 30N–50N).

aviation model provided the initial and boundary conditions for these MM5 runs. In addition the winds in the MM5 were relaxed to the NCEP analysis using the Newtonian relaxation approach [*Grell*, 1993]. The short integration times of the MM5 (30 hours) combined with the relaxation procedure ensure that the meteorological fields produced within the MM5 are close to the NCEP analysis.

[46] **Acknowledgments.** The authors would like to thank J.-F. Lamarque and M. Barth for their comments on the manuscript and Wei Wang for the assistance with the MM5 model. The National Center for Atmospheric Research is sponsored by the National Science Foundation.

References

Abbatt, J. P. D., Interaction of HNO_3 with water-ice surfaces at temperatures of the free troposphere, *Geophys. Res. Lett.*, *24*, 1479–1482, 1997.

Allen, D. J., et al., Transport-induced interannual variability of carbon monoxide determined using a chemistry and transport model, *J. Geophys. Res.*, *101*, 28,655–28,669, 1996.

Angevine, W. M., M. Trainer, S. A. McKeen, and C. M. Berkowitz, Mesoscale meteorology of the New England coast, Gulf of Maine,

and Nova Scotia: Overview, *J. Geophys. Res.*, *101*, 28,893–28,901, 1996a.

Angevine, W. M., M. P. Buhr, J. S. Holloway, M. Trainer, D. D. Parrish, J. I. MacPherson, G. L. Kok, R. D. Schillawski, and D. H. Bowlby, Local meteorological features affecting chemical measurements at a North Atlantic coastal site, *J. Geophys. Res.*, *101*, 28,935–28,946, 1996b.

Atkinson, R., D. L. Baulch, R. A. Cox, R. F. Hampson, J. A. Kerr, M. J. Rossi, and J. Troe, Evaluated kinetic, photochemical and heterogeneous data for atmospheric chemistry: Supplement V - IUPAC Subcommittee on Gas Kinetic Data Evaluation for Atmospheric Chemistry, *J. Phys. Chem. Ref. Data*, *26*, 521–1011, 1997.

Atlas, E., B. Ridley, and C. Cantrell, The Tropospheric Ozone Production About the Spring Equinox experiment: Introduction, *J. Geophys. Res.*, doi:10.1029/2002JD003172, in press, 2003.

Barrie, L. A., Arctic Air Pollution: An overview of current knowledge, *Atmos. Environ.*, *20*, 643–663, 1986.

Barrie, L. A., and R. M. Hoff, Five years of air chemistry observations in the Canadian Arctic, *Atmos. Environ.*, *19*, 1995–2010, 1985.

Barrie, L. A., J. W. Bottenheim, and W. R. Hart, Polar Sunrise Experiment 1992 (PSE 1992): Preface, *J. Geophys. Res.*, *99*, 25,313–25,314, 1994.

Barth, M. C., P. J. Rasch, J. T. Kiehl, C. M. Benkovitz, and S. E. Schwartz, Sulfur chemistry in the National Center for Atmospheric Research Community Climate Model: Description, evaluation, features and sensitivity to aqueous chemistry, *J. Geophys. Res.*, *105*, 1387–1415, 2000.

Blake, N. J., D. R. Blake, B. C. Sive, A. S. Katzenstein, S. Meinardi, O. W. Wingenter, E. L. Atlas, F. Flocke, B. A. Ridley, and F. S. Rowland, The seasonal evolution of NMHCs and light alkyl nitrates at mid to high northern latitudes during TOPSE, *J. Geophys. Res.*, *108*(4), 8359, doi:10.1029/2001JD001467, 2003.

Blake, D. R., and S. Rowland, Global atmospheric concentration and source strength of ethane, *Nature*, *321*, 231, 1986.

Brasseur, G. P., D. A. Hauglustaine, S. Walters, P. J. Rasch, J.-F. Muller, C. Granier, and X. X. Tie, MOZART, a global chemical transport model for ozone and related chemical tracers, 1, Model description, *J. Geophys. Res.*, *103*, 28,265–28,289, 1998.

Brown, S. S., R. K. Talukdar, and A. R. Ravishankara, Reconsideration of the rate constant for the reaction of hydroxyl radicals with nitric acid, *J. Phys. Chem. A*, *103*, 3031–3037, 1999.

Carlson, T. N., Speculations on the movement of polluted air to the Arctic, *Atmos. Environ.*, *15*, 1473–1477, 1981.

Carter, W. P. L., and R. Atkinson, Development and evaluation of a detailed mechanism for the atmospheric reactions of isoprene and NO_x, *Int. J. Kinetics*, *28*, 497–530, 1996.

Cavalieri, D., P. Gloerson, and J. Zwally, 1990–March 2000 DMSP SSM/I Daily Polar Gridded Sea Ice Concentrations (digital media), edited by J. Maslanik and J. Stroeve, Nat. Snow and Ice Data Cent., Boulder, Colo., 2002.

Comiso, J., 1990–March 2000 DMSP SSM/I Daily Polar Gridded Sea Ice Concentrations (digital media), edited by J. Maslanik and J. Stroeve, Nat. Snow and Ice Data Cent., Boulder, Colo., 2002.

Eberhard, J., and C. J. Howard, Rate coefficients for the reactions of some C-3 to C-5 hydrocarbon peroxy radicals with NO, *J. Phys. Chem. A*, *101*, 3360–3366, 1997.

Gierczak, T., J. B. Burkholder, R. K. Talukdar, A. Mellouki, S. B. Barone, and A. R. Ravishankara, Atmospheric fate of methyl vinyl ketone and methacrolein, *J. Photochem. Photobiol. A. Chem.*, *110*, 1–10, 1997.

Giorgi, F., and W. L. Chameides, The rainout parameterization in a photochemical model, *J. Geophys. Res.*, *90*, 7872–7880, 1985.

Grell, G. A., Prognostic evaluation of assumptions used by cumulus parameterizations, *Mon. Wea. Rev.*, *121*, 764–787, 1993.

Grell, G. A., J. Dudhia, D. R. Stauffer, A description of the fifth generation Penn State/NCAR Mesoscale Model (MM5), *NCAR/TN-398+IA*, 116 pp., Nat. Cent. for Atmos. Res., Boulder, Colo., 1993.

Hallquist, M., D. J. Stewart, J. Baker, and R. A. Cox, Hydrolysis of N_2O_5 on submicron sulfuric acid aerosols, *J. Phys. Chem. A*, *104*, 3984–3990, 2000.

Hess, P. G., Model and measurement analysis of springtime transport and chemistry of tile Pacific basin, *J. Geophys. Res.*, *106*, 12,689–12,717, 2001.

Hess, P. G., S. Flocke, J.-F. Lamarque, M. C. Barth, and S. Madronich, Episodic modeling of the chemical structure of the troposphere as revealed during the spring MLOPEX 2 intensive, *J. Geophys. Res.*, *105*, 26,809–26,839, 2000.

Heymsfield, A. J., and G. M. McFarquhar, High albedos of cirrus in the tropical Pacific warm pool: microphysical interpretations from CEPEX and from Kwajalein, *Marshall Islands J. Atmos. Sci.*, *53*, 2424–2451, 1996.

Hong, S.-Y., and H.-L. Pan, Nonlocal boundary layer vertical diffusion in a medium-range forecast model, *Mon. Wea. Rev.*, *124*, 2322–2339, 1996.

Hoskins, B. J., and P. J. Valdes, On the existence of storm-tracks, *J. Atmos. Sci.*, *47*, 1854–1864, 1990.

Iversen, T., On the atmospheric transport of pollution to the Arctic, *Geophys. Res. Lett.*, *11*, 457–460, 1984.

Jobson, B. T., Z. Wu, and H. Niki, Seasonal trends of isoprene, C_2–C_5 alkanes, and acetylene at a remote boreal site in Canada, *J. Geophys. Res.*, *99*, 1589–1599, 1994.

Kiehl, J. T., T. L. Schneider, P. J. Rasch, M. C. Barth, and J. Wong, Radiative forcing due to sulfate aerosols from simulations with the National Center for Atmospheric Research Community Climate model, Version 3, *J. Geophys. Res.*, *105*, 1441–1457, 2000.

Lamarque, J.-F., and P. G. Hess, Model analysis of the temporal and geographical origin of the CO distribution during the TOPSE campaign, *J. Geophys. Res.*, *108*(D4), 8354, doi:10.1029/2002JD002077, 2003.

Levy, H., II, and W. J. Moxim, Examining the global impact of local/regional air pollution: The role of global chemical transport models, in *Air Pollution Modeling and its Application VII*, pp. 139–157, Plenum, New York, 1989.

Lowenthal, D. H., and K. A. Rahn, Regional sources of pollution aerosol at Barrow, Alaska, during winter 1979–1980 as deduced from elemental tracers, *Atmos. Environ.*, *19*, 2011–2024, 1985.

Niki, H., P. D. Maker, C. M. Savage, and L. P. Breitenbach, An FTIR study of mechanisms for HO radical initiated oxidation of C_2H_4 in the presence of NO: Detection of glycolaldehyde, *Chem. Phys. Lett.*, *80*, 499–503, 1981.

Novelli, P. C., K. A. Masarie, and P. M. Lang, Distributions and recent changes in tropospheric carbon monoxide in the lower troposphere, *J. Geophys. Res.*, *103*, 19,015–19,033, 1998.

Orlando, J. J., G. S. Tyndall, M. Bilde, C. Ferronato, T. J. Wallington, L. Vereecken, and J. Peeters, Laboratory study of the mechanism of OH- and Cl- initiated oxidation of ethylene, *J. Phys. Chem. A*, *102*, 8116–8123, 1998.

Orlando, J. J., G. S. Tyndall, and S. E. Paulson, Mechanism for the OH-initiated oxidation of methacrolein, *Geophys. Res. Let.*, *26*, 2191–2195, 1999.

Orlando, J. J., G. S. Tyndall, L. Vereecken, and J. Peeters, The atmospheric chemistry of the acetonoxy radical, *J. Phys., Chem. A*, *104*, 11,578–11,588, 2000.

Penkett, S. A., N. J. Blake, P. Lightman, A. R. W. Marsh, P. Anwyl, and G. Butcher, The seasonal variation of nonmethane hydrocarbons in the free troposphere over the North Atlantic Ocean: Possible evidence for extensive reaction of hydrocarbons with the nitrate radical, *J. Geophys. Res.*, *98*, 2865–2885, 1993.

Pickering, K. E., Y. Wang, W.-K. Tao, C. Price, and J.-F. Muller, Vertical distributions of lightning NO_x for use in regional and global chemical transport models, *J. Geophys. Res.*, *103*, 31,203–31,216, 1998.

Price, C., and D. Rind, A simple lightning parameterization for calculating global lightning distributions, *J. Geophys. Res.*, *97*, 9919–9933, 1992.

Raatz, W. E., and G. E. Shaw, Long-range transport of pollution aerosols into the Alaskan Arctic, *J. Clim. Appl. Met.*, *23*, 1052–1064, 1984.

Raatz, W. E., The climatology and meteorology of Arctic air pollution, in *Pollution of the Arctic Atmosphere*, edited by W. T. Sturges, pp. 13–42, Elsevier, New York, 1991.

Ridley, B. A., E. L. Atlas, J. G. Walega, G. L. Kok, T. A. Staffelbach, J. P. Greenberg, F. E. Grahek, P. G. Hess, and D. D. Montzka, Aircraft measurements made during the spring maximum of ozone over Hawaii: Peroxides, CO, O_3, NO_y, condensation nuclei, selected hydrocarbons, alkyl nitrates between 0.5- and 9-km altitude, *J. Geophys. Res.*, *102*, 18,935–18,961, 1997.

Ridley, B. A., et al., Ozone depletion events observed in the high latitude surface layer during the TOPSE aircraft program, *J. Geophys. Res.*, *108*(D4), 8356, doi:10.1029/2001JD001507, 2003.

Sander, S. P., et al., Chemical Kinetics and Photochemical Data for Use in Stratospheric Modeling: Supplement to Evaluation 12: Update of Key Reactions, *JPL Publ. 00-3*, Jet Propul. Lab., Pasadena. Calif., 2000.

Solberg, S., C. Dye, and N. Schmidbauer, Carbonyls and nonmethane hydrocarbons at rural European sites from the Mediterranean to the Arctic, *J. Atmos. Chem.*, *25*, 33–66, 1996.

Tie, X., et al., Effect of sulfate aerosols on tropospheric NOx and ozone budgets: model simulations and TOPSE evidence, *J. Geophys. Res.*, *108*(4), 8364, doi:10.1029/2001JD001508, 2003.

Tuazon, E. C., and R. Atkinson, A product study of the gas-phase reaction of methacrolein with the OH radical in the presence of NO_x, *Int. J. Chem. Kinet.*, *22*, 591–602, 1990.

Tyndall, G. S., R. A. Cox, C. Granier, R. Lesclaux, G. K. Moortgat, M. J. Pilling, A. R. Ravishankara, and T. J. Wallington, Atmospheric chemistry

of small organic peroxy radicals, *J. Geophys. Res.*, *106*, 12,157–12,182, 2001.

Villenave, E., and R. Lesclaux, Kinetics of the cross sections of CH_3O_2 and $C_2H_5O_2$ radicals with selected peroxy radicals, *J. Phys. Chem.*, *100*, 14,372–14,382, 1996.

Wahner, A., T. F. Mentel, and M. Sohn, Gas-phase reaction of N_2O_5 with water vapor: importance of heterogeneous hydrolysis of N_2O_5 and surface desorption of HNO_3 in a large teflon chamber, *Geophys. Res. Lett.*, *25*, 2169–2172, 1998.

Wollenhaupt, M., S. A. Carl, A. Horowitz, and J. N. Crowley, Rate coefficients for reaction of OH with acetone between 202 and 395 K, *J. Phys. Chem. A*, *104*, 2695–2705, 2000.

Young, V. L., B. N. Kieser, S. P. Chen, and H. Niki, Seasonal trends and local influences on nonmethane hydrocarbon concentration in the Canadian boreal forest, *J. Geophys. Res.*, *102*, 5913–5918, 1997.

Zhu, L., D. Kellis, and C.-F. Ding, Photolysis of glyoxal at 193, 248, 308 and 351 nm, *Chem. Phys. Lett.*, *257*, 487–491, 1996.

Zondlo, M. A., S. B. Barone, and M. A. Tolbert, Uptake of HNO_3 on ice under upper tropospheric conditions, *Geophys. Res. Lett.*, *24*, 1391–1394, 1997.

D. Blake, Department of Chemistry, 570 Rowland Hall, University of California, Irvine, CA 92697, USA.

L. Emmons, P. Hess, J. Orlando, and L. Smith, National Center for Atmospheric Research, 1850 Table Mesa Drive, Boulder, CO 80307, USA.

A. Klonecki, NOVELTIS, Parc Technologique du Canal, 2, Avenue de l'Europe, 31520 Ramonville-Saint-Agne, France. (klonecki@lsce.saclay.cea.fr)